Fatigue on shape memory alloys: Experimental observations and constitutive modeling

Vanderson M. Dornelas [a], Sergio A. Oliveira [b], Marcelo A. Savi [a], Pedro Manuel Calas Lopes Pacheco [b], Luis Felipe G. de Souza [b]

[a] *Center for Nonlinear Mechanics, Department of Mechanical Engineering, Universidade Federal do Rio de Janeiro, COPPE, P.O. Box 68.503, 21.941.972 – Rio de Janeiro, RJ, Brazil*
[b] *Department of Mechanical Engineering, CEFET/RJ – Centro Federal de Educação Tecnológica Celso Suckow da Fonseca, 20.271.110 – Rio de Janeiro, RJ, Brazil*

ARTICLE INFO

ABSTRACT

This paper deals with the fatigue of shape memory alloys considering both experimental and theoretical approaches. Initially, experimental tests are performed considering NiTi pseudoelastic wires subjected to different load conditions. Functional and structural fatigue are investigated considering situations related to phase transformations and plastic behavior. Afterward, experimental macroscopic observations are employed to propose a three-dimensional constitutive model to describe the general thermomechanical behavior of shape memory alloys, including functional and structural fatigue with a continuum damage perspective. An equivalent critical damage is proposed in order to define the fatigue life of shape memory alloys, considering different behaviors of martensitic and austenitic phases. Numerical simulations are compared with experimental data showing the capabilities of the proposed model. Results show that the model responses are in close agreement with experimental data, including fatigue life predictions.

1. Introduction

Shape memory alloys (SMAs) are metals with thermomechanical behaviors associated with solid-solid martensitic phase transformations, which are characterized by shear displacement of atoms on a scale below the interatomic distance promoting large deformations and small volume changes (Yamauchi et al., 2011). Due to their unique properties (Cisse et al., 2016), SMAs have a large potential for applications in different areas such as biomedical, automotive, oil and gas, robotics, and aerospace fields (Lagoudas, 2008; Petrini & Migliavacca, 2011; Barbarino et al., 2014; Mohd Jani et al., 2014). In many applications, these materials are subjected to cyclic loads and therefore the study of fatigue is an important issue that must be considered in the modeling of SMAs.

Fatigue can be defined as the progressive deterioration of materials under cyclic loading that leads to failure (Suresh, 1998). In general, fatigue can be classified into low cycle fatigue (material accumulates plastic strains during the cyclic loading) and high cycle fatigue (material undergoes only elastic strains). Concerning

SMAs, it is usually subdivided into functional and structural fatigue (Eggeler et al., 2004). Structural fatigue is a classical definition associated with the element rupture due to the growth and propagation of microcracks. On the other hand, functional fatigue represents the reduction of functional properties during cyclic loadings, such as phase transformation capacity, hysteresis loop size, and phase transformation critical stresses. Since phase transformations can be induced to either stress or temperature, it is expected that SMA presents either mechanical or thermal functional fatigue.

In recent years, many researchers have proposed studies on fatigue of SMAs. Considering experimental analysis, Scirè Mammano and Dragoni (2014) characterized NiTi wires subjected to different loadings representing typical working conditions of real actuators employed in several applications. Mahtabi et al. (2015a) investigated the effect of mean strain on the fatigue behavior of NiTi alloys showing its detrimental effects at least for large strain amplitudes. Qin et al. (2019) investigated functional and structural fatigue on SMA wires under various maximum heating temperatures using a thermomechanical fatigue experimental setup. The influence of the maximum heating temperature on fatigue life, strain evolution, and failure type were discussed and a model to

simulate the plastic evolution behavior was proposed. Tyc et al. (2016) developed an experimental study using NiTi wires subjected to different types of cold work and heat treatments in order to investigate the influence of the microstructure obtained on the functional and structural fatigue.

Predki et al. (2006) investigated the mechanical response of pseudoelastic NiTi alloys subjected to cyclic torsional loading, emphasizing the effect of torsional loading on the stress shear hysteresis. On the other hand, de Oliveira Ramos et al. (2018) performed a set of cyclic tension tests using NiTi wires to evaluate functional and structural fatigue under different loading conditions. Both cases observed a progressive decrease in the hysteresis loop with the increase of the number of cycles as a result of the evolution of functional fatigue. Qiu et al. (2019) investigated the interaction between the rate-dependent transformation ratcheting and fatigue failure of superelastic NiTi alloys subjected to uniaxial and torsional stress-controlled fatigue tests. Results showed that the uniaxial loading promotes more transformation ratcheting when compared to torsional ones, on the other hand, the torsional fatigue lives are significantly greater than the uniaxial ones. In addition, other studies are available in the literature considering an experimental approach as, for instance: Figueiredo et al. (2009), Lagoudas et al. (2009), Kang et al. (2012), Song et al. (2015a), Zheng et al. (2017) and Jaureguizahar et al. (2018).

Fatigue failure modeling of SMAs has been investigated in recent years, essentially considering two approaches: based on Coffin-Manson's empirical law as presented by (Tobushi et al. (2000), Runciman et al. (2011), Maletta et al. (2012), Maletta et al. (2014)) and (Kollerov et al., 2013); and based on dissipated energy as developed by Moumni et al. (2005), Song et al. (2015b), Zhang et al. (2016a), Song et al. (2017), Zhang et al. (2017) and Zhang et al. (2019).

Critical revisions about functional and structural fatigue on SMAs are available in the literature. In this regard, Pelton (2011) proposed a review of NiTi alloys subjected to cyclic transformations induced by thermal and mechanical loadings emphasizing the effects caused on the microstructure of these materials. Kang & Song (2015) reviewed the main advances achieved in experimental and theoretical analyses of structural fatigue in NiTi alloys. Mahtabi et al. (2015b) presented a general review of the fatigue behavior in NiTi alloys addressing the main factors that modify the fatigue strength of these materials. Finally, Moumni et al. (2018) documented a general approach to study structural fatigue of shape memory alloys, considering low cycle fatigue and high cycle fatigue.

In order to explore all the potentialities of SMAs, there is an increasing interest in the development of constitutive models to describe the thermomechanical behaviors of these materials. Lagoudas (2008) and Paiva & Savi (2006) presented a general overview of the macroscopic thermomechanical description of SMAs. Thermomechanical coupling is an important topic for the SMA description, including anisotropy and stress-compression asymmetry (Monteiro et al., 2009; Paiva et al., 2005). Chatziathanasiou et al. (2016) developed a three-dimensional thermodynamical coupled model that captures the particular behavior of SMAs subjected to non-proportional thermomechanical loadings. A new approach to describe the martensitic reorientation mechanism had been introduced associated with a new method to account forward and reverse transformations. Viet et al. (2019) developed an analytical asymmetry model for superelastic cantilever SMA beams. The deformation of the beam is described based on Timoshenko beam theory using constitutive relations that account for asymmetric shape memory alloy response in tension and compression.

Barrera et al. (2014) presented a macroscopic constitutive model being able to reproduce the effects caused by functional fatigue in SMAs. Zhang et al. (2016b) proposed a constitutive model based on a more accurate subdivision of martensite volume frac-

tions as internal variables to control the evolution of functional damage during phase transformation.

Hartl et al. (2014) developed a three-dimensional constitutive model to describe the functional and structural fatigue of SMA actuators subjected to a large number of cycles. The model was based on the continuum damage mechanics to represent the structural fatigue, and the evolution of transformation induced plasticity to describe functional fatigue. Chemisky et al. (2018) proposed a new phenomenological model that considers the coupling between accumulation of damage and the transformation induced plasticity to describe functional and structural fatigue in SMAs. Phillips et al. (2019) developed a constitutive model to examine the evolution of internal damage of SMA actuators based on experimental investigation. Dornelas et al. (2020) presented a three-dimensional constitutive macroscopic model to describe functional fatigue in shape memory alloys within the framework of continuous damage. Essentially, a new internal variable was included into the previous model proposed by Oliveira et al. (2016), Oliveira et al. (2018) together with new evolution laws.

The present work proposes a three-dimensional constitutive model to describe the general thermomechanical behavior of shape memory alloys, including functional and structural fatigue. This model is an extension of the one proposed by Dornelas et al. (2020), including structural fatigue into the analysis. Local continuum damage approach is of concern, employing two damage variables for functional and structural damage. Compared with the constitutive models available in the literature, the main advantage is the ability to describe different thermomechanical behaviors associated with SMAs, including functional and structural fatigue, being able to describe different thermomechanical loading conditions and several related phenomena together. The proposition of this model is guided by experimental tests developed in order to highlight the main macroscopic thermomechanical fatigue behaviors of SMAs. Experimental tests are performed considering NiTi pseudoelastic wires subjected to different loading conditions. A novel equivalent critical damage is proposed in order to define the fatigue life of SMAs, considering different behaviors of martensitic and austenitic phases. The ability of the proposed model to describe SMA fatigue is established comparing numerical simulations with experimental data. Results show that the model presents responses that are in close agreement with experimental data, including fatigue life predictions. Besides, the influence of structural damage on the loss of actuation performance of SMAs is evaluated. Structural damage acts together with functional damage modifying the functional characteristics, with a preponderant effect of functional damage.

After this introduction, the present work is structured as follows. Section 2 presents an experimental investigation establishing the main characteristics of the macroscopic thermomechanical behavior of NiTi with respect to functional and structural fatigue. The constitutive model is developed in Section 3. Numerical simulations and their comparison with experimental data are presented in Section 4. The conclusions are presented in Section 5.

2. Experimental observations

This section aims to analyze the main macroscopic characteristics of the thermomechanical fatigue behavior of shape memory alloys through experimental observations. The experimental methodology is divided into three main parts: experimental setup, Section 2.1; material characterization, Section 2.2; and fatigue tests, Section 2.3.

2.1. Experimental setup

Experimental tests are conducted using a pseudoelastic Ni56Ti44 (wt.%) wire in the as-received condition, manufactured

by Sandinox biomaterials according to ASTM F2063-18 (2018) specifications, with a circular section with diameter of 1.3 mm (±0.0354). The wire thermomechanical condition is polished drawing and annealed. Surface condition corresponds to the finishing condition as provided by the manufacturer, presenting a smooth surface, free of marks, scratches or indentations that can compromise fatigue behavior. In general, results where failures occurred close to the grips are discarded. In order to carry out the material characterization, quasi-static tensile tests are performed using an electro-mechanical testing machine, Instron 5882, employing a 30 kN static load cell and strain measurement based on the displacement with gage length of 100 mm. Besides, phase transformation temperatures are evaluated using a differential scanning calorimeter (DSC), NETZSCH Maia 200 F3. Fatigue tests are performed using a servo-hydraulic fatigue testing system, Instron 8801, with pneumatic grips and a 5 kN load cell and strain measurement based on the displacement with gage length of 50 mm.

2.2. Material characterization

Quasi-static tensile tests are carried out to define the stress-strain response and the functional parameters of the SMA. Initially, the stress-strain response is analyzed following the ASTM F2516-14 (2014) standard. Therefore, a wire with a diameter of 1.3 mm and 100 mm of gauge length is of concern, subjected to a strain rate of 0.02 mm/min until the sample reaches a 6% strain. Afterward, the sample is unloaded at the same rate to less than 7 MPa and then loaded again until its rupture at a rate of 0.2 mm/min. Fig. 1 shows the stress-strain curve highlighting four regions: (I) full austenitic microstructure with a linear elastic behavior; (II) phase transformation response; (III) full detwinned martensite microstructure with a linear elastic behavior; (IV) plastic response, where the yield surface is reached, and the sample failure.

The functional parameters are estimated by considering a quasi-static cyclic tensile test with peak stress of 900 MPa and a frequency of 0.0028 Hz. Fig. 2 (a) presents stress-strain curves with 30 cycles for this test while Fig. 2 (b) presents the first cycle analysis where it is identified some material properties. Elastic moduli for austenitic and martensitic phases (E^A and E^M) are identified by calculating the angular coefficients of the lines that pass through the elastic regions of austenite and martensite, respectively. The methodology follows the same idea presented by Savi et al. (2015) to reduce the influence of instability effects related to
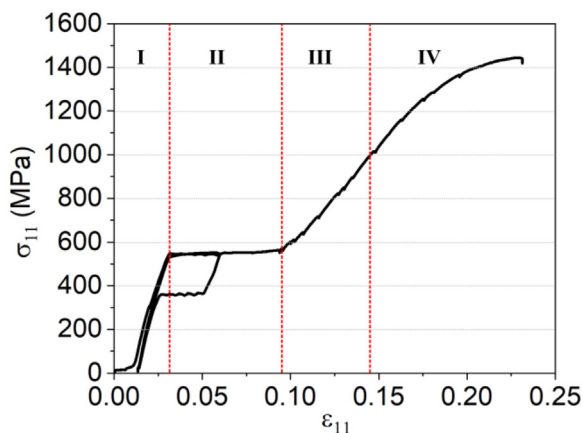
experimental measurements at the beginning of the test and at the load reversal regions. Therefore, the slope is calculated considering selected points in the region close to the end of the elastic region, before the start of the phase transformation. Phase transformation critical stress for direct (σ^{M_s} and σ^{M_f}) and reverse (σ^{A_s} and σ^{A_f}) phase transformations are determined using the tangent method, which consists of determining the intersection of the tangent lines to the regions where the phase transformations start and finish. This analysis can be performed in different cycles.

The analysis of phase transformation temperatures is performed through DSC tests using three virgin wire samples (A1, A2, A3). During the tests, the sample is heated from room temperature to 120 °C and then cooled to −120 °C. After that, this cycle is repeated. Fig. 3 shows results of these tests highlighting the average temperatures and their respective standard deviations. During heating, there are two regions of phase transformation (martensite → R-Phase and R-Phase → austenite) and a peak of transformation during cooling (austenite → martensite). After the DSC test, a macroscopic verification is performed considering stress-strain curves for high, ambient temperature and low temperature behavior. Note that the sample presents pseudolasticity at ambient temperature and shape memory effect for low temperature behavior.

2.3. Fatigue tests

After the characterization, fatigue tests are carried out in order to evaluate the functional and structural fatigue presented by SMAs during cyclic loads. Different stress-controlled tensile loadings and frequencies are considered for this aim. The definition of the mechanical loadings are made according to a previous characterization presented in Fig. 1. In this regard, different tests are defined according to the four regions, evaluating the fatigue behavior under different conditions. The choice of the test frequencies is based on thermomechanical coupling aspects. During the phase transformations, exothermic reactions occur during the direct transformation (austenite → martensite) and endothermic reactions in the reverse transformation (martensite → austenite). Therefore, the test frequency is defined based on thermal equilibrium, which means that phase transformation latent heat have a proper balance with convection capacity. This balance defines the maximum test frequency, and the tests are guided by experimental results due to de Oliveira Ramos et al. (2018), presenting a maximum frequency of 2 Hz. As presented in de Oliveira Ramos et al. (2018) and in Zhang et al. (2017), low frequency stress controlled tests are interesting for fatigue analysis since they are related to frequency independent fatigue lifetime determination. In addition, SMA thermomechanical characteristics introduces difficulties related to the control system. A series of tests are performed in order to define proper adjustments of the PID controller values for each test frequency. The best choices produce results without significant variations of the actuator speed or control disturbances.

Fatigue tests are conducted at room temperature, assuming that mechanical cyclic loading that varies linearly from zero to a maximum value and then back to a residual stress, close to zero. Three samples with 50 mm of gauge length are used for each test (A1, A2, A3) but Figures are plotted considering results with the largest number of cycles until rupture. Table 1 presents the number of cycles to failure (N_f) for all samples analyzed, in addition to the average number of cycles to failure ($\bar{N_f}$) and their respective standard deviations (s). Besides, Table 1 shows the loading regions in which the samples are submitted (presented in Fig. 1) corresponding to the maximum applied stresses.

Initially, four distinct loading processes are treated within the yield surface. Basically, two different maximum stress values are
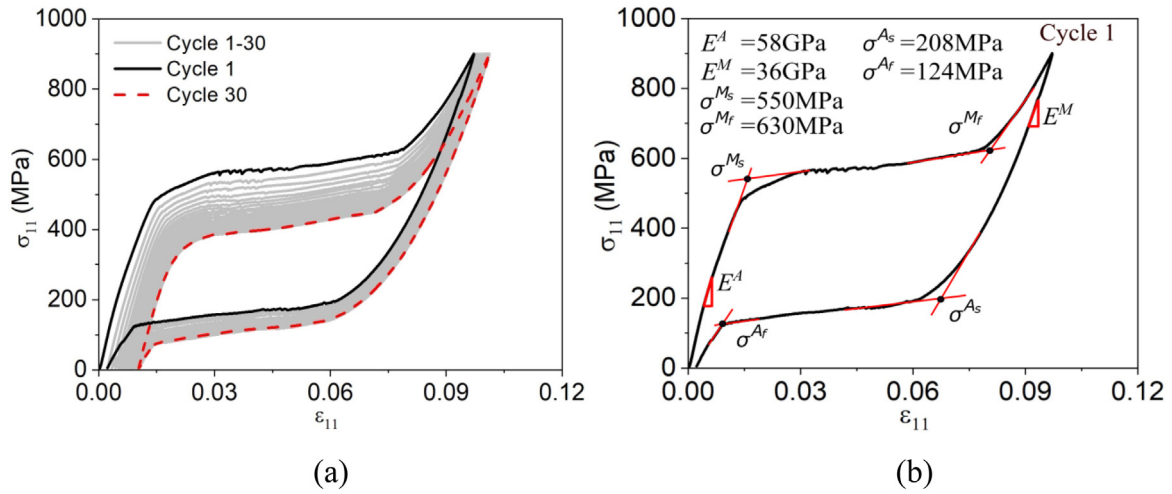

Fig. 1. Quasi-static tensile tests of a pseudoelastic NiTi wire defining four regions: (I) full austenitic microstructure with a linear elastic behavior; (II) phase transformation response; (III) full detwinned martensite microstructure with a linear elastic behavior; (IV) plastic response, where the yield surface is reached, and the sample failure.

Fig. 2. Quasi-static tensile tests of a pseudoelastic NiTi wire. (a) cyclic stress-strain response presenting 30 cycles; (b) functional parameters evaluated from the first cycle.
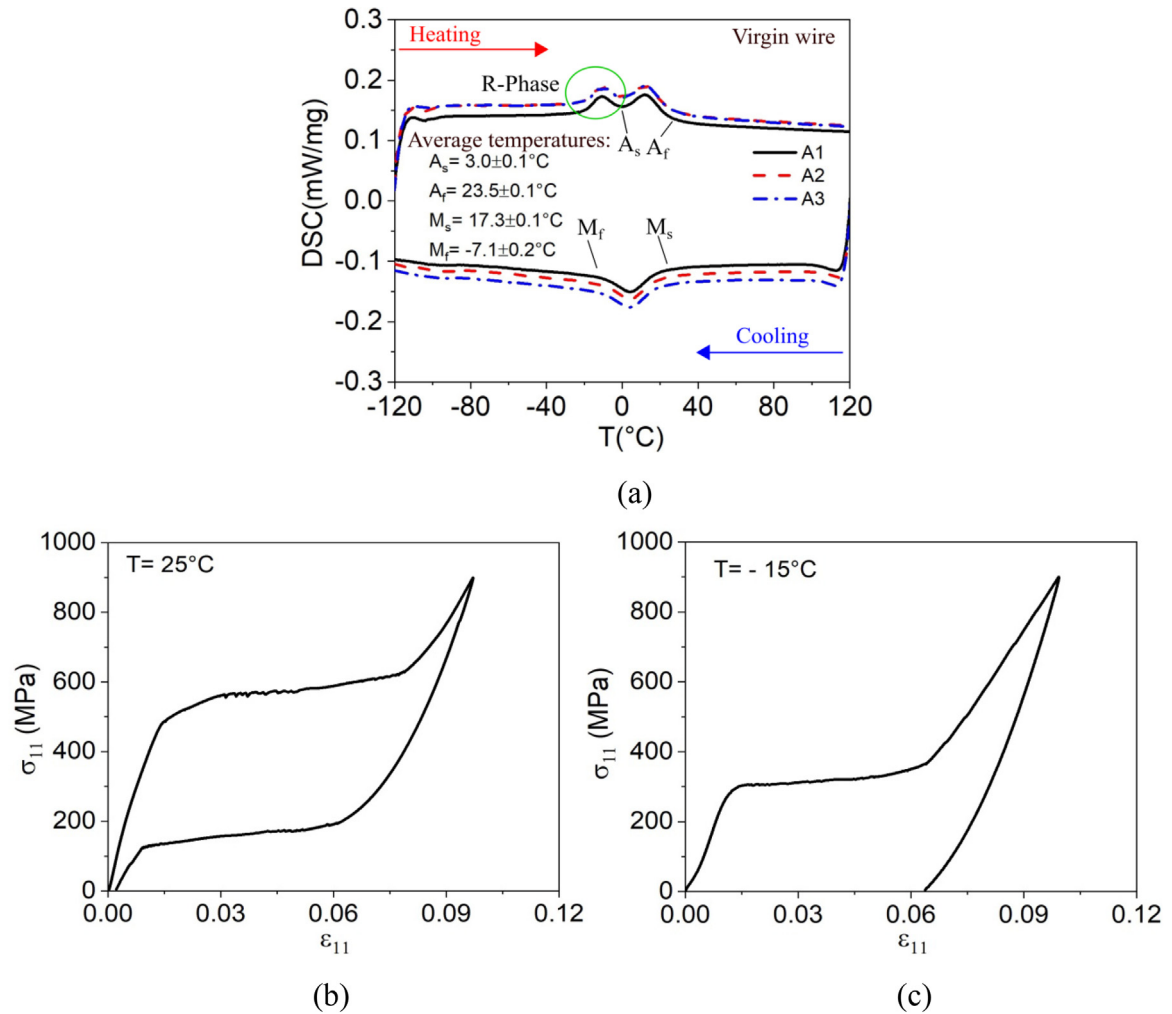

Fig. 3. Phase transformation temperatures and the macroscopic verification through stress-strain curves. (a) DSC thermal analysis of the virgin NiTi wire. (b) High temperature stress-strain curve showing pseudoelasticity. (c) Low temperature stress-strain curve showing shape memory effect.

considered, $\sigma_{max} = 680$ and $\sigma_{max} = 750$ MPa, and two different frequencies, 0.25 and 1 Hz. Fig. 4 presents stress-strain curves for all the cases characterizing a pseudoelastic behavior. Fig. 4 (a) and (c) show results considering the frequency of 0.25 Hz, while Fig. 4 (b)

and (d) show results for the frequency of 1 Hz. At the beginning of the loading process, there is a variation of the maximum and minimum stress due to the adjustment of the loading control imposed on the testing machine. Hence, the sample does not exhibit com-

Table 1
Number of cycles to failure (N_f) of the NiTi SMA wire.

Frequency (Hz)	σ_{max}(MPa)	Load region	N_f(A1)	N_f(A2)	N_f(A3)	$\bar{N}_f \pm s$
	680	I, II, III	3147	2003	3093	2748 ± 645
0.25	750	I, II, III	1875	2308	2293	2158 ± 246
	1150	I, II, III, IV	3084	3157	1748	2663 ± 793
	680	I, II, III	1671	2789	1183	1181 ± 823
1	750	I, II, III	1514	2569	1709	1930 ± 561
	1150	I, II, III, IV	4379	3626	2205	3238 ± 1376
2	530	I	26,805	33,757	35,060	31,874 ± 4438
1, 2	900	III	27,220	13,358	20,267	20,282 ± 6931

plete phase transformation during the first cycles. The first cycles are essentially characterized by the transformation induced plasticity (TRIP) that can be defined as the plastic strain arising from phase transformation processes involving volume and/or shape changes without reaches the yield surface (Oliveira et al., 2018). The transformation induced plasticity tends to stabilize after some cycles. It is also noticeable that the increase of stress level promotes a more severe functional property change. This result indicates that increasing the applied stress, a greater accumulation of functional fatigue occurs, causing a loss of actuation performance after a certain number of cycles. This aspect can be clearly observed in Fig. 5 that shows the evolution of phase transformation

critical stresses σ^{M_s} and σ^{A_s} as a function of the number of cycles. Note a reduction of the critical stress transformation with the increase of the number of cycles. On the other hand, despite the dispersion of the number of cycles until failure presented by the tests (Table 1), results do not show a significant variation of the number of cycles until failure, remaining within the range of 10^3 cycles, considering the increase of the applied stress level.

Concerning the frequency, it can be observed that the frequency increase (0.25 Hz → 1 Hz) causes a change of the hysteresis loop shape, as shown in Fig. 4. This change promotes a modification of the evolution of phase transformation critical stresses, as observed in Fig. 5. Note that for the frequency of 1 Hz, σ^{M_s} has the same
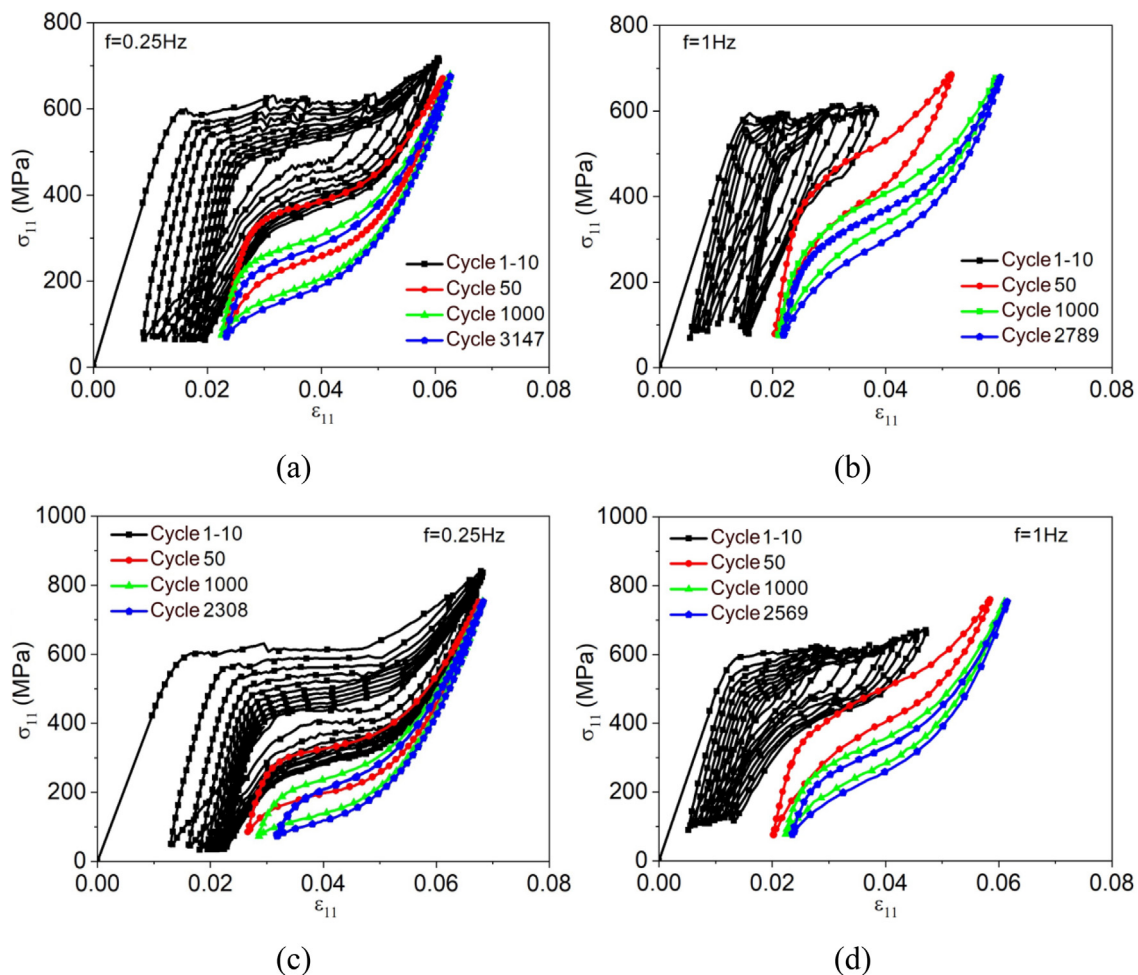

Fig. 4. Pseudoelastic behavior for the NiTi SMA wires during fatigue tests. (a) σ_{max} = 680 MPa, 0.25 Hz; (b) σ_{max} = 680 MPa, 1 Hz; (c) σ_{max} = 750 MPa, 0.25 Hz; (d) σ_{max} = 750 MPa, 1 Hz.

Fig. 5. Evolution of the critical stress transformation σ^{M_s} and σ^{A_s}. (a) σ_{max} = 680 MPa, 0.25 Hz; (b) σ_{max} = 680 MPa, 1 Hz; (c) σ_{max} = 750 MPa, 0.25 Hz; (c) σ_{max} = 750 MPa, 1 Hz.
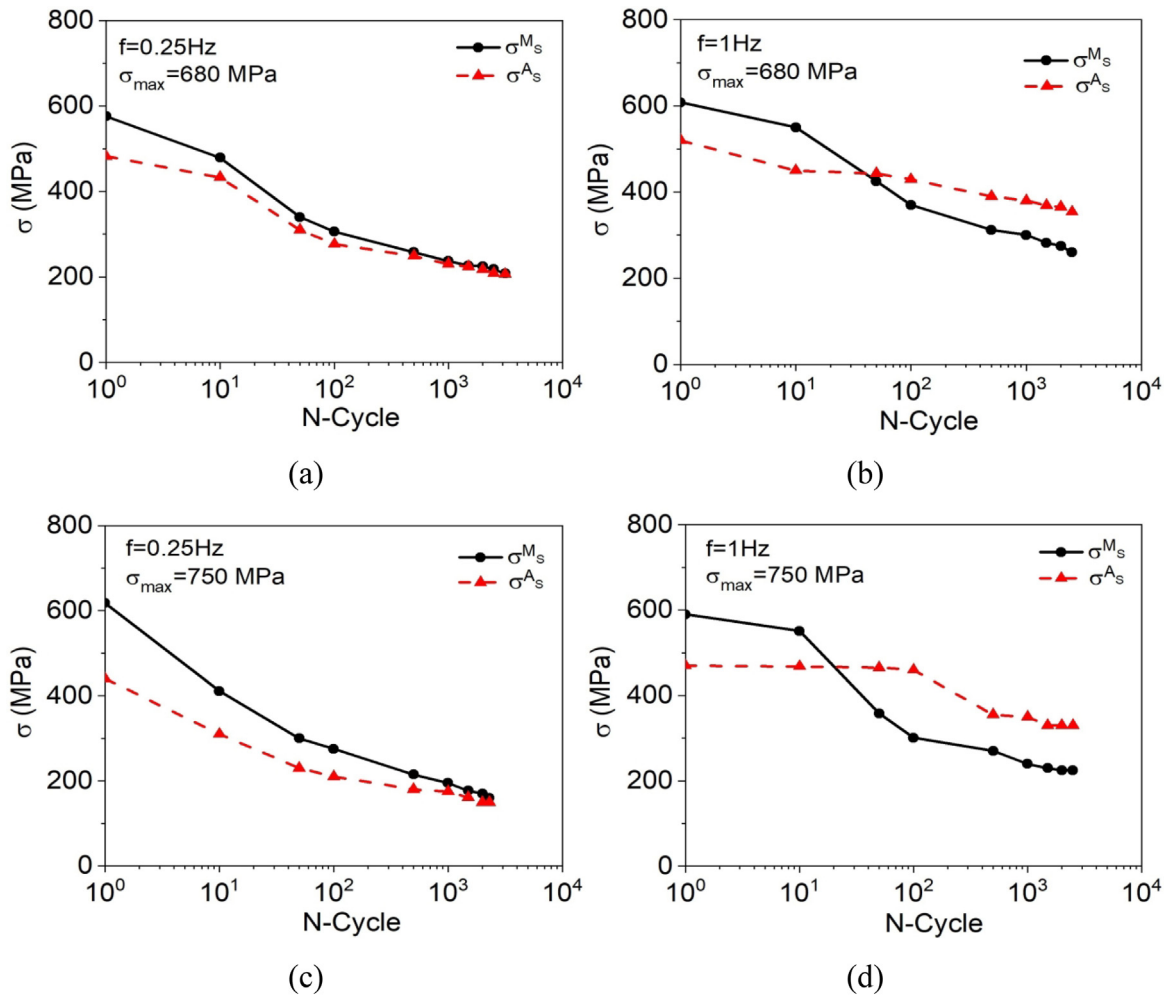
value of σ^{A_s} after a certain number of cycles, assuming a higher value in the following cycles. Besides, according to Zhang et al. (2017), the increase of the frequency during tests tends to promote a decrease in the number of cycles until failure.

The effect of classical plasticity on SMA fatigue life is now of concern considering a loading process that reaches the yield surface. Fig. 6 shows results of a test with a peak stress of 1150 MPa, with the same frequencies previously proposed. It is
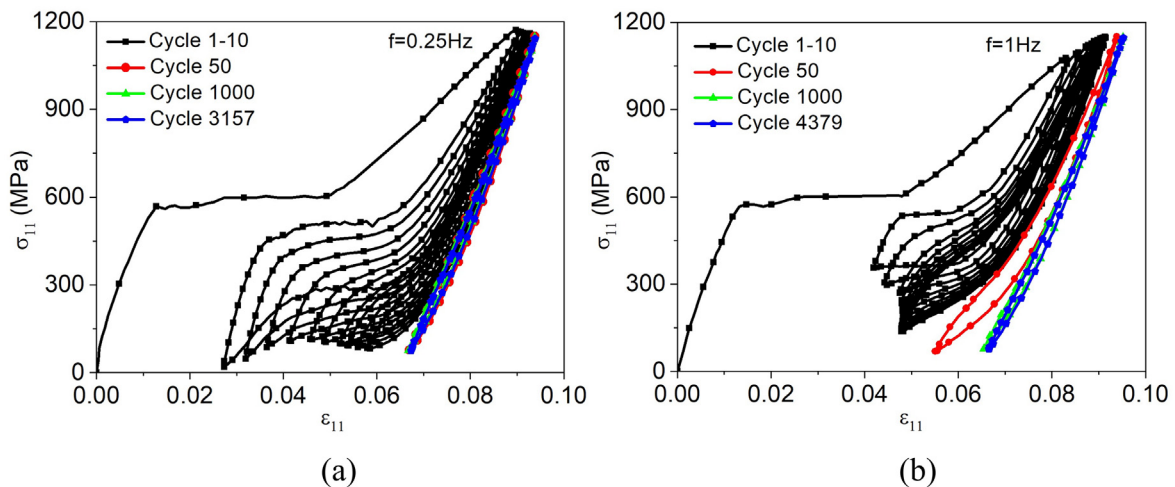

Fig. 6. Pseudoelastic behavior for the NiTi SMA wires during fatigue tests. (a) σ_{max} = 1150 MPa, 0.25 Hz; (b) σ_{max} = 1150 MPa, 1 Hz.

observed that the plasticity causes a loss of actuation performance after a few cycles, for both frequencies. On the other hand, the number of cycles until failure remains within the range presented on the previous tests, which means that it does not have a significant influence.

SMA fatigue related to elastic responses, without phase transformations, is now in focus. Based on that, loading processes promote the SMA sample to be within the regions (I) or (III) of Fig. 1. This kind of behavior is related to a situation where cyclic loads do not promote loss of actuation due to functional fatigue and therefore, can be understood as a situation where structural fatigue is preponderant. The first test is performed considering elastic cyclic loading in the austenitic phase, varying between 230 and 530 MPa (region I) at a frequency of 2 Hz. Fig. 7 (a) presents stress-strain curve showing a maximum strain of 1%, without phase transformations. Besides, results suggest that the absence of phase transformations promotes an increase of the fatigue life of the material when compared to the previous results where phase transformations take place.

Fig. 7 (b) presents results considering a martensitic elastic response, associated with region (III). Initially, SMA sample undergoes a training process with 50 loading cycles at a frequency of 1 Hz. After that point, the sample is subjected to a loading varying between 600 and 900 MPa, within the elastic region of the martensitic phase, at a frequency of 2 Hz. After the training process, an identical stress amplitude proposed in the previous test is performed. Once again, it is observed an increase of fatigue life due to the absence of phase transformations.

Cyclic loads affect phase transformation temperatures, which can be evaluated using DSC tests. Fig. 8 shows a comparison between the phase transformation temperatures for the virgin wire and after the different fatigue tests carried out through this section. Note that the virgin wire, Fig. 8 (a), presents three regions where the phase transformations occur. When the material is subjected to a load within the elastic region of austenite, Fig. 8 (b), there is a small increase of phase transformation temperatures. Fig. 8 (c) – (e) show results considering the different loading processes where phase transformations occur. There is a reduction of the transformation peaks (except for the martensite → R-Phase peak, which remains approximately constant) and a progressive increase of the phase transformation temperatures of the material depending on the applied load. Fig. 8 (f) shows results of the martensitic elastic response that is associated with the 50 cycles training at a

maximum tension of 900 MPa, followed by a cyclic loading within the elastic phase of the martensite. Similar behavior of the previous one is observed, with an increase of the phase transformation temperatures. In conclusion, the comparison shows a dependence of the phase transformation temperatures with the applied load. Tests subjected to phase transformations present a progressively increase of temperature with the increase of the stress load level.

3. Constitutive model

The constitutive modeling of shape memory alloys can be performed through the formalism of generalized standard materials as proposed by Halphen & Nguyen (1975), and Lemaitre & Chaboche (1990). Based on that, the thermodynamic state of the material is established by the Helmholtz free energy density, Ψ, and the pseudo-potential of dissipation, Φ. Based on Helmholtz free energy density, thermodynamic forces are defined for each state variable. Complementary laws are established based on the pseudo-potential of dissipation. For more details about this procedure, see Dornelas et al. (2020).

A new three-dimensional constitutive model is proposed for the description of the SMA thermomechanical behavior, including functional and structural fatigue. The model is an extension of the model proposed by Dornelas et al. (2020) considering a new internal variable associated with structural damage. Therefore, the proposed model considers two internal variables to describe functional and structural fatigue in order to represent the thermomechanical behavior of SMAs under different loading perspectives.

Under these assumptions, consider the elastic strain tensor, ε_{ij}^e, the temperature, T, and three macroscopic phases, represented by their volume fraction: β^+ and β^- associated with martensitic variants, and β^A, related to austenitic phase. Classical plasticity is described by considering the plastic strain tensor, ε_{ij}^p, kinematic hardening ϑ, and isotropic hardening, ς_{ij}. Transformation induced plasticity (TRIP) is treated with the following variables: TRIP strain, ε_{ij}^{trip}, and saturation variables for each phase, ξ^+, ξ^- and ξ^A.

The three-dimensional description considers an equivalent strain field, Γ, representing a phase transformation inductor responsible for the definition of the induced martensitic variant, as defined follows:

$$\Gamma = \frac{1}{3}\varepsilon_{kk}^e + \frac{2}{3}\sqrt{3J_2^e}\,\text{sign}(\varepsilon_{kk}^e) \tag{1}$$
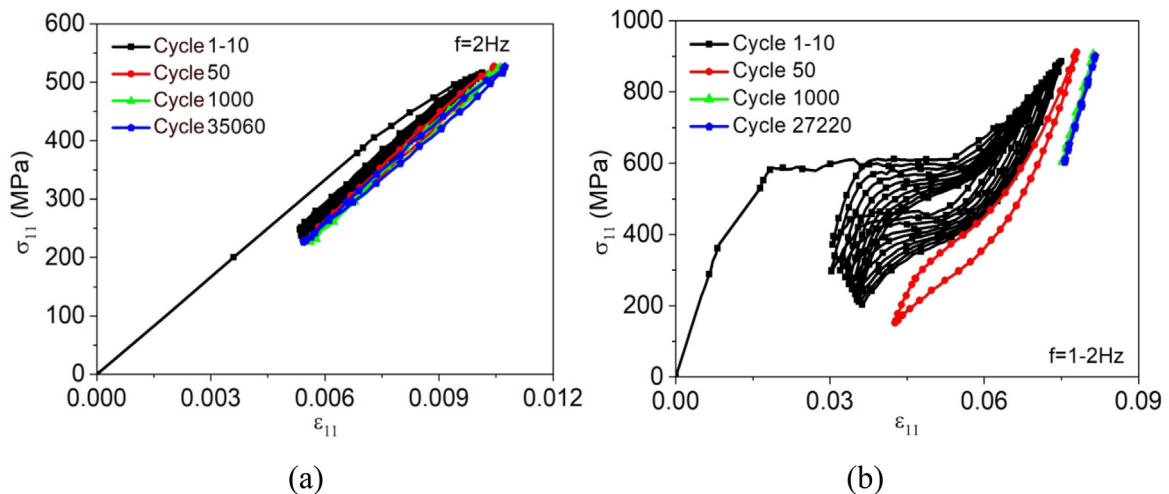

(a)   (b)

Fig. 7. Pseudoelastic behavior for the NiTi SMA wires during fatigue tests. (a) $\sigma_{max} = 530$ MPa, 2 Hz; (b) $\sigma_{max} = 900$ MPa, 1–2 Hz.
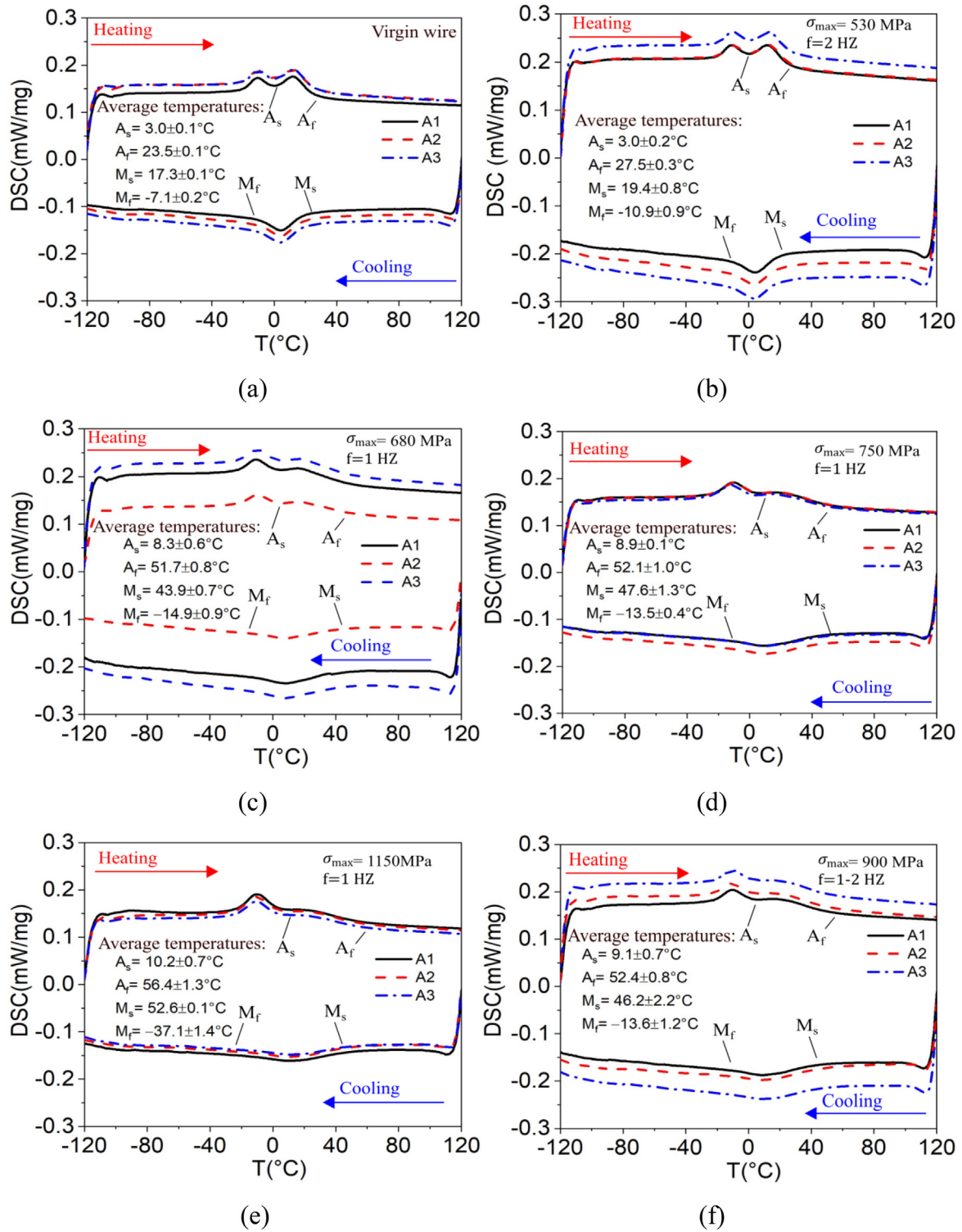
Fig. 8. Phase transformation temperatures, comparative between virgin material and subjected to different loading levels. (a) Virgin sample; (b) σ_{max} = 530 MPa; (c) σ_{max} = 680 MPa; (d) σ_{max} = 750 MPa; (e) σ_{max} = 1150 MPa; (f) σ_{max} = 900 MPa.

In the previous equation, ε_{kk}^e and J_2^e represents the volumetric and deviatoric terms, that are respectively given by:

$$\varepsilon_{kk}^e = \varepsilon_{11}^e + \varepsilon_{22}^e + \varepsilon_{33}^e \tag{2}$$

$$
\begin{aligned}
J_2^e &= \frac{1}{6}\widehat{\varepsilon}_{ij}^e\widehat{\varepsilon}_{ij}^e \\
&= \frac{1}{6}\left\{\left(\varepsilon_{11}^e - \varepsilon_{22}^e\right)^2 + \left(\varepsilon_{22}^e - \varepsilon_{33}^e\right)^2 + \left(\varepsilon_{33}^e - \varepsilon_{11}^e\right)^2 + 6[\left(\varepsilon_{12}^e\right)^2 + \right. \\
&\quad \left. +\left(\varepsilon_{13}^e\right)^2 + \left(\varepsilon_{23}^e\right)^2]\right\}
\end{aligned}
\tag{3}
$$

The deviatoric elastic strain is given by:

$$\widehat{\varepsilon}_{ij}^e = \varepsilon_{ij}^e - \frac{1}{3}\varepsilon_{kk}^e\delta_{ij} \tag{4}$$

and

$$\text{sign}(\varepsilon_{kk}^e) = \begin{cases} +1, & \text{if } \varepsilon_{kk}^e \geq 0 \\ \\ -1, & \text{if } \varepsilon_{kk}^e < 0 \end{cases} \tag{5}$$

where δ_{ij} is the Kronecker delta and ε_{ij}^e is the elastic strain.

Fatigue description follows the same approach developed by Dornelas et al. (2020) based on local continuum damage and therefore, size effects are not captured by the model. Functional and structural fatigue are treated considering structural damage, D_e, which represents continuum damage that describes the degree of deterioration of the material, from a structural point of view. $D_e = 0$ represents the virgin state and $0 \leq D_e < 1$ characterizes the damaged state. In addition, functional damage considers the internal variable D_f that represents the loss of functional performance being associated with damaged material state. The damaged state is characterized by $0 \leq D_f < 1$, where $D_f = 0$ represents the undamaged material and $D_f = 1$ is a material state that is not able to perform any actuation. (Lemaitre & Chaboche, 1990).

Based on that, the thermomechanical behavior of SMAs, including functional and structural fatigue, is presented in the sequence.

Stress-strain-temperature relation:

$$\sigma_{ij} = (1 - D_e)\left(E_{ijkl}\varepsilon_{kl}^e\right) + \alpha\omega_{ij}\left(\beta^- - \beta^+\right) - \Omega_{ij}(T - T_0) \tag{6}$$

Evolution equations for the volume fractions:

$$
\begin{aligned}
\dot{\beta}^+ &= \frac{1}{\eta^+}\left[\alpha\Gamma + (1 - D_f)\Lambda + P^+ - \alpha_{ijkl}^h r_{kl}\Omega_{ij}(T - T_0) - \eta^l K\vartheta \right. \\
&\quad \left. -\eta_{ij}^K\frac{\varsigma_{ij}}{H} - \kappa_\pi^+\right] + \kappa_\chi^+
\end{aligned}
\tag{7}
$$

$$
\begin{aligned}
\dot{\beta}^- &= \frac{1}{\eta^-}\left[-\alpha\Gamma + (1 - D_f)\Lambda + P^- + \alpha_{ijkl}^h r_{kl}\Omega_{ij}(T - T_0) - \eta^l K\vartheta - \eta_{ij}^K\frac{\varsigma_{ij}}{H} - \kappa_\pi^-\right] \\
&\quad + \kappa_\chi^-
\end{aligned}
\tag{8}
$$

$$
\begin{aligned}
\dot{\beta}^A &= \frac{1}{\eta^A}\left[(1 - D_f)\Lambda^\aleph + P^A + \varepsilon_{ij}^e\left(\Omega_{ij}^A - \Omega_{ij}^M\right)(T - T_0) \right. \\
&\quad \left. -\frac{1}{2}\left(K^A - K^M\right)\vartheta^2 - \left(\frac{1}{2H^A} - \frac{1}{2H^M}\right)\varsigma_{ij}\varsigma_{ij} + \eta^l K\vartheta + \eta_{ij}^K\frac{\varsigma_{ij}}{H} - \kappa_\pi^A\right] \\
&\quad + \kappa_\chi^A
\end{aligned}
\tag{9}
$$

Evolution equations for plasticity:

$$\dot{\varepsilon}_{ij}^p = \gamma\frac{\widehat{\sigma}_{ij} - \varsigma_{ij}}{\|\widehat{\sigma}_{ij} - \varsigma_{ij}\|} \tag{10}$$

$$\dot{\vartheta} = \sqrt{\frac{2}{3}}\gamma + \eta^l\left(\dot{\beta}^+ + \dot{\beta}^- + \dot{\beta}^A\right) \tag{11}$$

$$\dot{\varsigma}_{ij} = \frac{2}{3}H\dot{\varepsilon}_{ij}^p + \eta_{ij}^K\left(\dot{\beta}^+ + \dot{\beta}^- + \dot{\beta}^A\right) \tag{12}$$

Evolution equations for TRIP:

$$
\begin{aligned}
\dot{\varepsilon}_{ij}^{trip} &= 2\sigma_{ij}\left\{\left(M_{13}\beta^+ + M_{31}\beta^A\right)\dot{\beta}^+ + \left(M_{32}\beta^- + M_{23}\beta^A\right)\dot{\beta}^- \right. \\
&\quad \left. + \left[M_{43}\beta^A + M_{34}\left(1 - \beta^+ - \beta^- - \beta^A\right)\right]\dot{\beta}^A\right\}
\end{aligned}
\tag{13}
$$

$$\dot{\xi}^+ = |\dot{\beta}^+|; \dot{\xi}^- = |\dot{\beta}^-|; \dot{\xi}^A = |\dot{\beta}^A| \tag{14}$$

Evolution equation for functional damage:

$$\dot{D}_f = (C_1 + C_2\Gamma^\sigma)^{C_3}\left(|\dot{\beta}^+| + |\dot{\beta}^-| + |\dot{\beta}^A|\right) \tag{15}$$

Evolution equation for structural damage:

$$\dot{D}_e = (C_4 + C_5\Gamma^\sigma)^{C_6}\left|\dot{\varepsilon}_{ij}^e\right| + (C_7 + C_8\Gamma^\sigma)^{C_9}\left|\dot{\varepsilon}_{ij}^p\right| \tag{16}$$

Yield surface and its conditions:

$$f = \|\widehat{\sigma}_{ij} - \varsigma_{ij}\| - \sqrt{\frac{2}{3}}(\sigma_Y - K\vartheta) \tag{17}$$

$$\gamma \geq 0; f \leq 0 \text{ and } \gamma f = 0; \gamma\dot{f} = 0 \text{ if } f = 0 \tag{18}$$

where γ is the plastic multiplier.

These equations use a series of parameters that are related to different physical processes including thermo-elasto-plasticity, phase transformation, and transformation induced plasticity.

Damage description considers the function $(C_1 + C_2\Gamma^\sigma)^{C_3}$ to provide the relation between functional damage and accumulated phase transformation. Similarly, structural damage considers the functions $(C_4 + C_5\Gamma^\sigma)^{C_6}$ and $(C_7 + C_8\Gamma^\sigma)^{C_9}$, respectively related to elastic and elasto-plastic fatigue. These functions are inspired on the classical theory of continuum damage proposed by Lemaitre & Chaboche (1990) considering the parameters C_{1-3} to control the evolution of functional damage and C_{4-9} to control the evolution of structural damage. Different, complex phenomena are expressed in this description and the proposed expressions provide a proper macroscopic description of all of them.

The fatigue life of SMAs is predicted by considering the definition of a novel equivalent critical damage, D_c, which takes into account the effects caused by the evolution of functional and structural damage. Once again, several complex behaviors are involved in this description and the proposed expression provides a macroscopic representation of all of these phenomena. Among these, it should be pointed out the different structural fatigue behaviors that can be observed for austenite and martensite (Jaureguizahar et al., 2016; Zhang et al., 2017; Sgambitterra et al., 2019) and, therefore, the proposed model considers that the evolution of the structural damage depends on the volume fraction. Under these assumptions, the following expression is adopted for the critical damage that defines the SMA fatigue life:

$$D_c = \left[\zeta^A\beta^A + \zeta^+\beta^+ + \zeta^-\beta^-\right]D_e + D_f \tag{19}$$

where ζ^A, ζ^+ and ζ^- are parameters employed to represent the austenite and martensite structural fatigue strength, respectively. Based on that, the failure is assumed to be the state at which D_c reaches a critical value, D_c^{crit}, which can be estimated through experimental observations. The definition of the critical value is evaluated observing the stress-strain slope at the final cycles, before the failure.

Considering the thermoelastic parameters, E_{ijkl} is the elastic tensor and Ω_{ij} is related to the thermal expansion coefficient. Both tensors can be represented by the same general form:

$$E_{ijkl} = E_{ijkl}^M + \beta^A \left(E_{ijkl}^A - E_{ijkl}^M \right); \quad \Omega_{ij} = \Omega_{ij}^M + \beta^A \left(\Omega_{ij}^A - \Omega_{ij}^M \right).$$

The constitutive model employs different parameters to describe the phase transformation process. In this respect, α is a parameter that controls the height of the stress-strain hysteresis loop; Λ and $\Lambda^\aleph$ are temperature functions that define the critical stress value for the phase transformation.

$$\Lambda = 2\Lambda^M = \begin{cases} -L_0^\pm + \frac{L^\pm}{T^M}\left(T - T^M\right) \text{ if } T > T^M \\ -L_0^\pm \text{ if } T \le T^M \end{cases} \tag{20}$$

$$\Lambda^\aleph = \Lambda^M + \Lambda^A = \begin{cases} -L_0^A + \frac{L^A}{T^M}\left(T - T^M\right) \text{ if } T > T^M \\ -L_0^A \text{ if } T \le T^M \end{cases} \tag{21}$$

where T^M is the temperature below which the martensitic phase becomes stable for a stress-free state; Λ^M and Λ^A are the stress phase transformation values for martensite and austenite, respectively.

Furthermore, α_{ijkl}^h is a fourth-order tensor that controls the stress-strain hysteresis loop width; r_{kl} is a symmetric second-order tensor associated with the loading history:

$$r_{kl} = \begin{cases} +1, \text{ if } \sigma_{kl} > 0 \\ 0, \text{ if } \sigma_{kl} = 0 \\ -1, \text{ if } \sigma_{kl} < 0 \end{cases} \tag{22}$$

The internal dissipation during the phase transformation is represented by the parameters η^+, η^- and η^A.

Concerning classical plasticity parameters, K is plastic modulus; H is the kinematic hardening modulus. These parameters are defined considering a rule of mixture: $K = K^M + \beta^A \left(K^A - K^M \right)$ and $\frac{1}{H} = \frac{1}{H^M} + \beta^A \left(\frac{1}{H^A} - \frac{1}{H^M} \right)$, similar to the presented previously for E_{ijkl} and Ω_{ij}. In addition, η^I defines the coupling between phase transformation and isotropic hardening. The coupling between phase transformation and kinematic hardening is defined by the second-order tensor, η_{ij}^K. The yield surface is defined by the yield stress σ_Y that has different values for austenitic and martensitic phases.

TRIP effect is described by the parameters $M_{13}, M_{31}, M_{23}, M_{32}, M_{34}$ and M_{43}. These parameters have a saturation characteristic defined from TRIP variables:

$M_{ij} = \widehat{M}_{ij} \exp\left(-m^M \xi^i\right)$, where m^M is a saturation parameter. In addition, other parameters as $\alpha, L_o^+, L_o^-, L_o^A, L^+, L^-, L^A$, also presents a saturation characteristic as follows:

$$(\ ) = \widehat{(\ )} \left[\frac{n + \exp\left(-m^{(\ )} \xi^\pm\right)}{n+1} \right] \tag{23}$$

where n is used to obtain an appropriate adjustment and $m^{(\ )}$ is a saturation parameter.

Auxiliary variables are also employed to present the thermodynamical forces, being defined as follows:

$$\omega_{ij} = \frac{1}{3}\delta_{ij} + \left[\frac{3\varepsilon_{ij}^e - \varepsilon_{kk}^e \delta_{ij}}{3\sqrt{3J_2^e}} \right] \text{sign}(\varepsilon_{kk}^e) \tag{24}$$

$$P^+ = (1 - D_e)\left(E_{ijkl}\varepsilon_{kl}^e \alpha_{ijpq}^h r_{pq} \right) + \alpha(\beta^- - \beta^+)\left[\frac{1}{3}\alpha_{iikl}^h r_{kl} + \frac{2P^\alpha}{\sqrt{3J_2^e}} \text{sign}(\varepsilon_{kk}^e) \right] \tag{25}$$

$$P^- = -(1 - D_e)\left(E_{ijkl}\varepsilon_{kl}^e \alpha_{ijpq}^h r_{pq} \right) - \alpha(\beta^- - \beta^+)\left[\frac{1}{3}\alpha_{iikl}^h r_{kl} + \frac{2P^\alpha}{\sqrt{3J_2^e}} \text{sign}(\varepsilon_{kk}^e) \right] \tag{26}$$

$$P^A = -\frac{1}{2}(1 - D_e)\left(E_{ijkl}^A - E_{ijkl}^M \right)\varepsilon_{ij}^e \varepsilon_{kl}^e \tag{27}$$

$$P^\alpha = \frac{\alpha_S^h}{6}\left[(r_{11} - r_{22})(\varepsilon_{11}^e - \varepsilon_{22}^e) + (r_{22} - r_{33})(\varepsilon_{22}^e - \varepsilon_{33}^e) + (r_{33} - r_{11})(\varepsilon_{33}^e - \varepsilon_{11}^e) + 6(r_{12}\varepsilon_{12}^e + r_{13}\varepsilon_{13}^e + r_{23}\varepsilon_{23}^e) \right] \tag{28}$$

Phase transformation constraints:

Internal constraints appear in the constitutive equations to define proper conditions for phase transformations. They can be represented by sub-differential of the indicator functions or by Lagrange multipliers, which are essentially described by projections on a convex set. In this regard, it is important to highlight $\kappa_\pi\left(\beta^+, \beta^-, \beta^A\right)$ that represents the phase coexistence constraints associated with the convex set π, which can be geometrically interpreted by the tetrahedron of volume fraction variables.
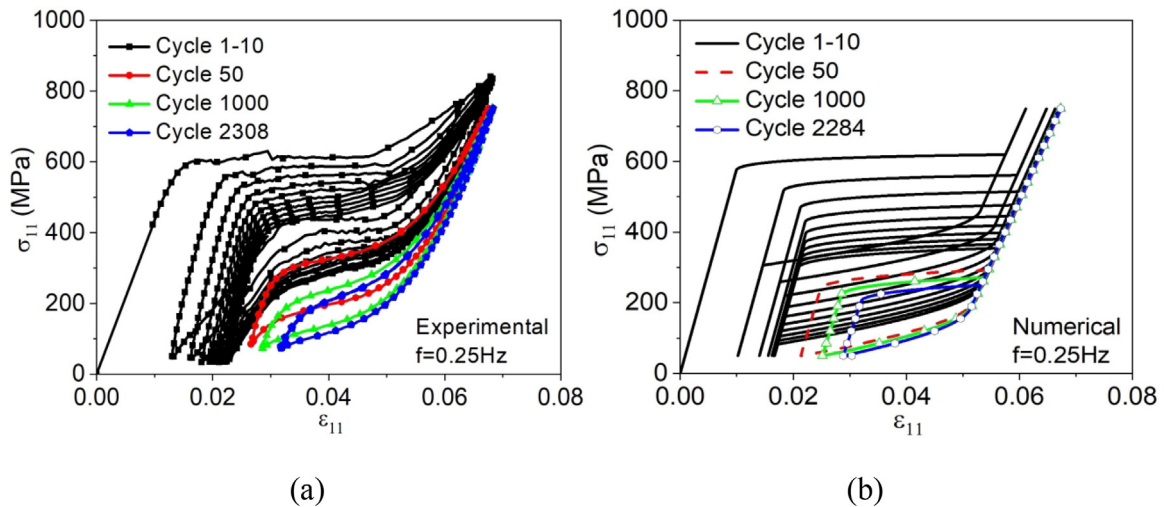

(a)

(b)

Fig. 9. Pseudoelastic behavior for the NiTi SMA wires during fatigue tests, $\sigma_{max} = 750$ MPa, 0.25 Hz. (a) experimental result; (b) numerical result.

Table 2
Parameters identified from experimental results for a NiTi wire.

| E^A (GPa)	E^M (GPa)	Ω^A (MPa/K)	Ω^M (MPa/K)	α_N^h(MPa)	$\widehat{\alpha}$(MPa)
58.0	36.0	0.74	0.17	0.028	100.0
$\widehat{L}_0^{\pm}$(MPa)	$\widehat{L}^{\pm}$(MPa)	$\widehat{L}_0^A$(MPa)	$\widehat{L}^A$(MPa)	$(\eta_L)_N$(MPa.s)	$(\eta_U)_N$(MPa.s)
6.00	5.00	0.60	105.50	0.10	0.80
$(\eta_L^A)_N$(MPa.s)	$(\eta_U^A)_N$(MPa.s)	T^M (K)	T^A (K)	σ_Y^M(GPa)	σ_Y^{Ai}(GPa)
0.10	0.80	266.0	297.0	0.30	1.15
σ_Y^{Af}(GPa)	K^A (GPa)	K^M (GPa)	H^A (GPa)	H^M (GPa)	η^I
0.60	1.4	0.4	4.0	1.1	−0.01
η^K	T^F (K)	$\widehat{M}_{13}$(GPa^{-1})	$\widehat{M}_{31}$(GPa^{-1})	$\widehat{M}_{32}$(GPa^{-1})	$\widehat{M}_{23}$(GPa^{-1})
−0.01	423.0	0.85	0.05	0.85	0.05
T^{trip}(K)	m^α	m^L	m^M	n	C_1
297.0	1.0×10^{-4}	0.1	0.4	0.7	5.0×10^{-6}
C_2	C_3	C_4	C_5	C_6	C_7
5.5×10^{-12}	1.58	5.0×10^{-12}	8.9×10^{-12}	5.0×10^{-12}	8.9×10^{-12}
C_8	C_9	ζ^A	ζ^+	D_c^{crit}	
1.58	1.58	3.38	0.87	0.16	
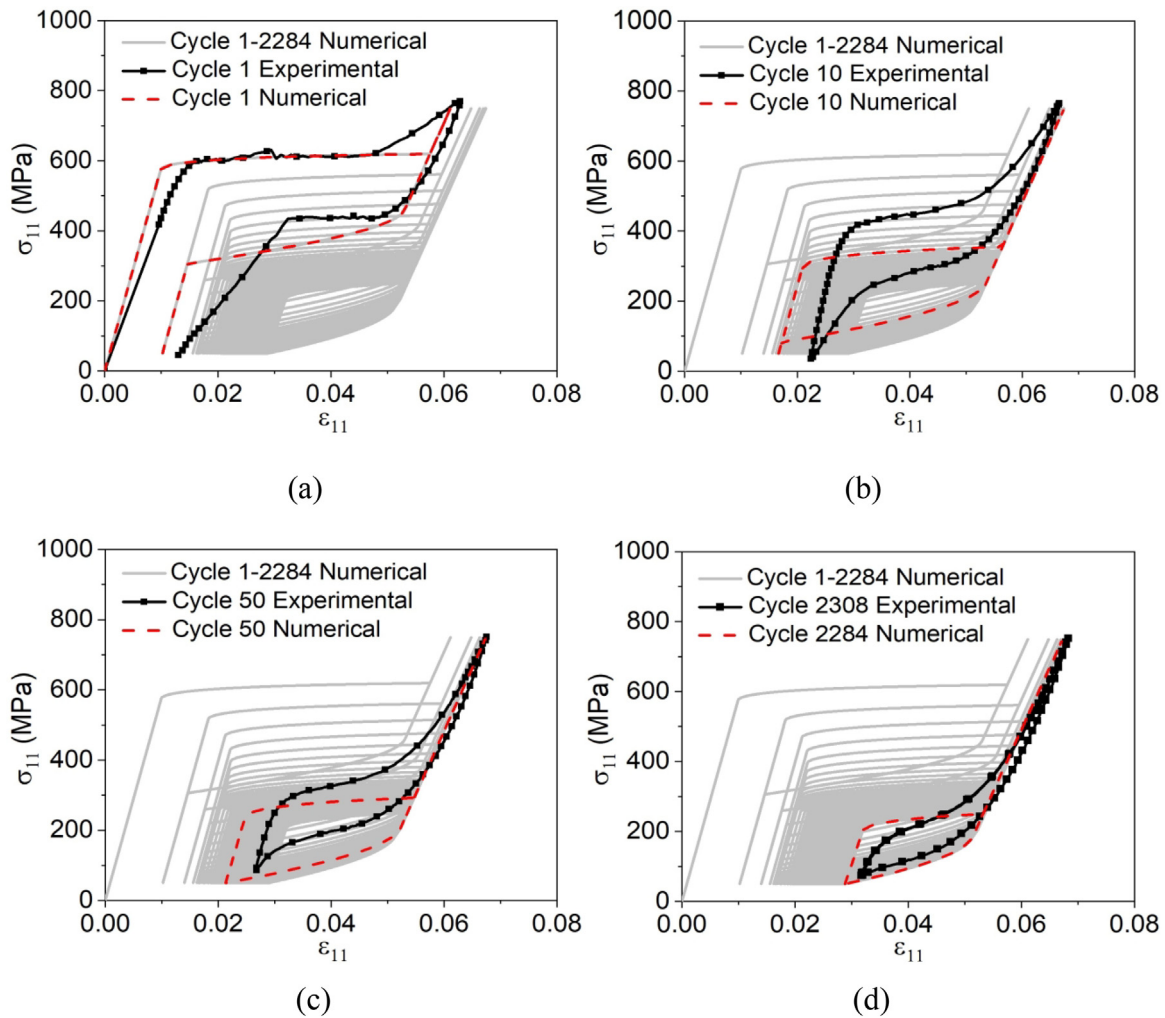
Fig. 10. Pseudoelastic behavior for the NiTi SMA wires during fatigue tests, $\sigma_{\max} = 750$ MPa, 0.25 Hz. Numerical-experimental comparative for different cycles: (a) cycle 1; (b) cycle 10; (c) cycle 50; (d) cycles 2308 (experimental) and 2284 (numerical).
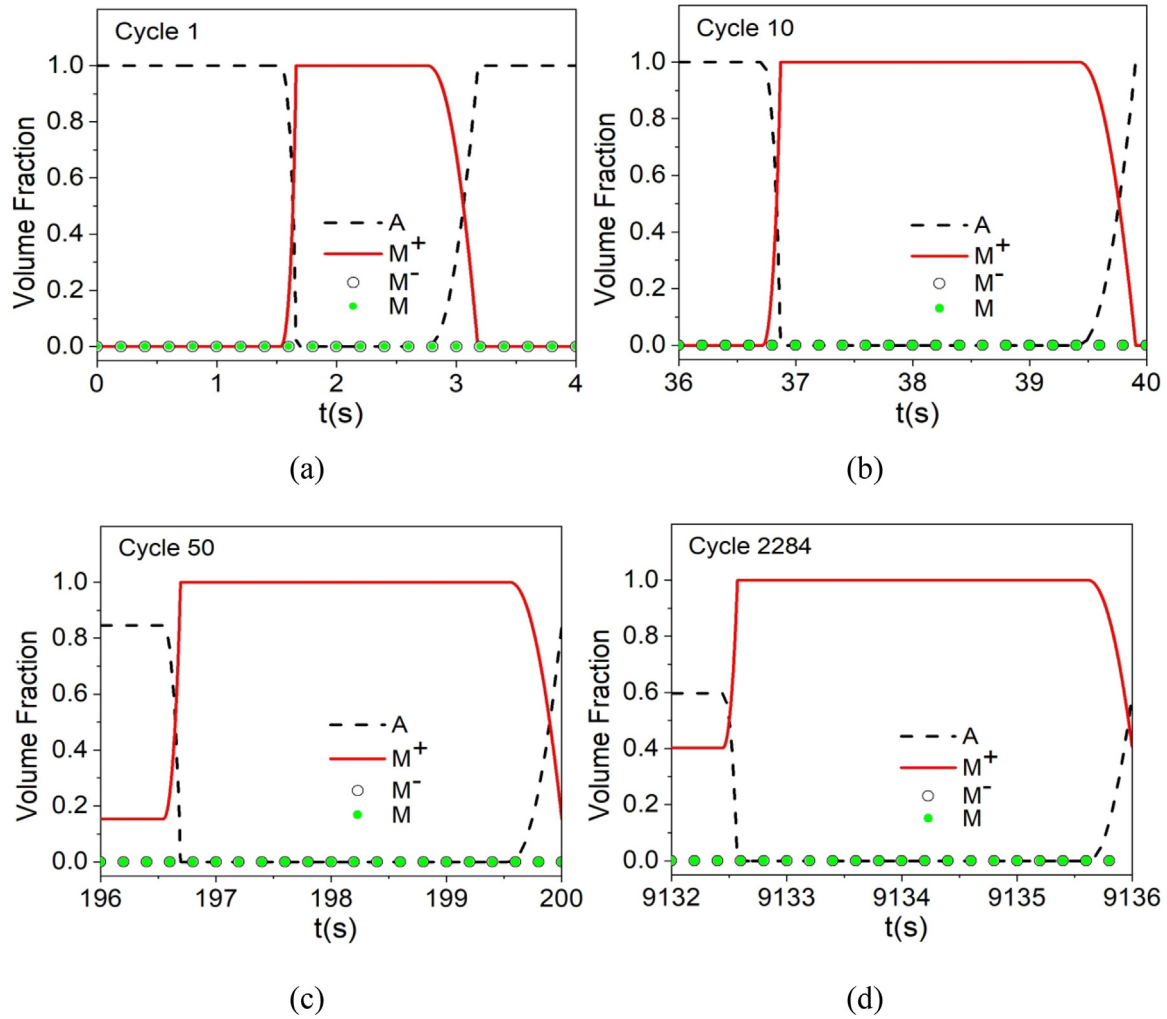
Fig. 11. Evolution of volume fractions through different cycles to evaluate functional and structural fatigue. (a) cycle 1; (b) cycle 10; (c) cycle 50; (d) cycle 2284.
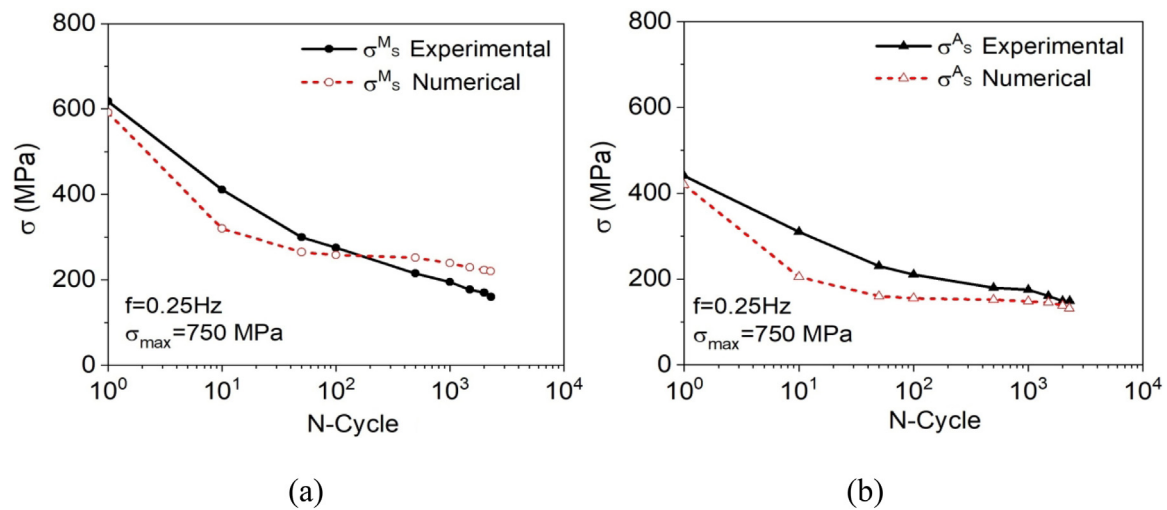

Fig. 12. Evolution of the critical stress transformation. Numerical-experimental comparative for $\sigma_{max} = 750$ MPa and f = 0.25 Hz. (a) σ^{M_s}; (b) σ^{A_s}.
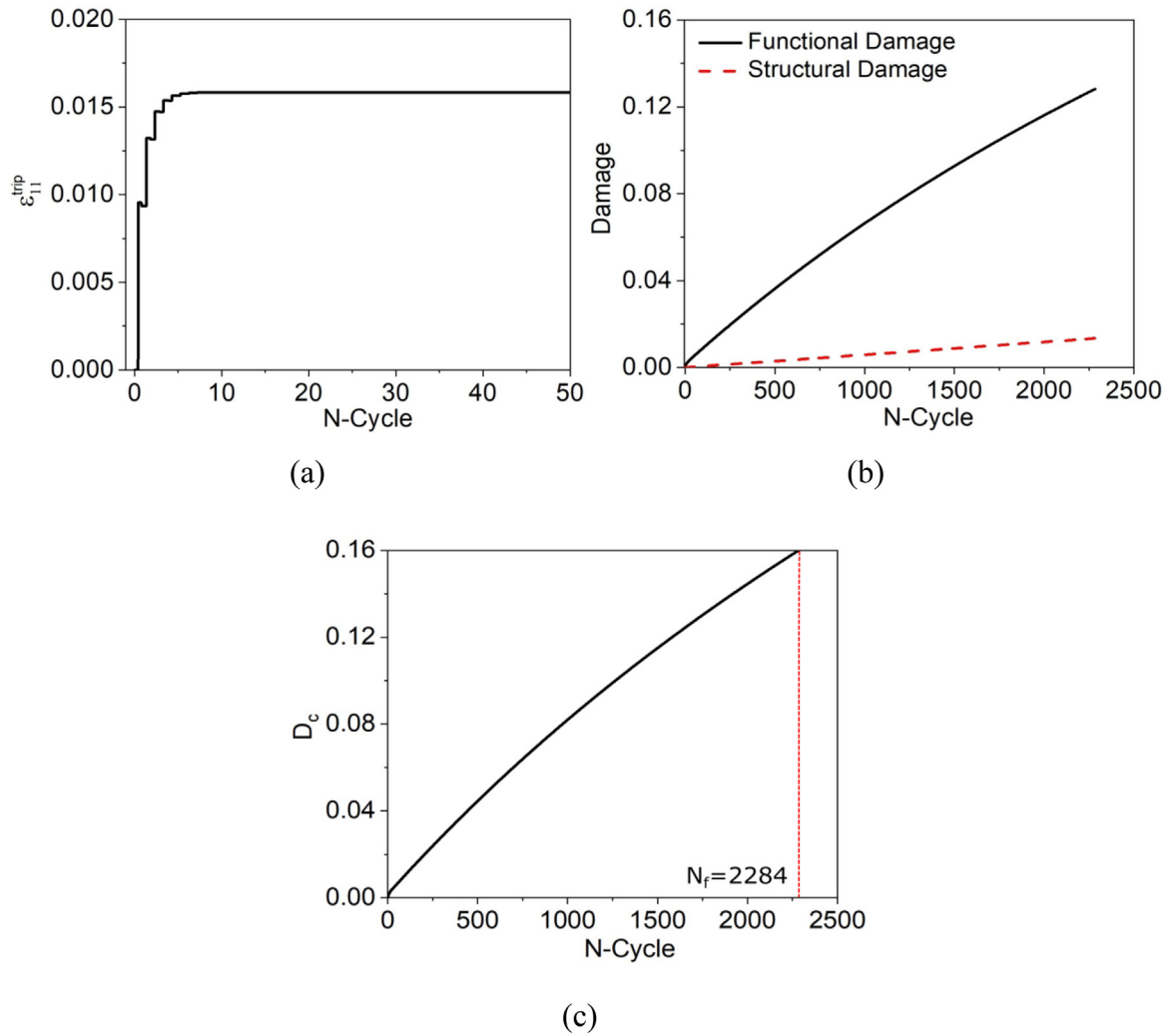
(a)

(b)

(c)

Fig. 13. TRIP strain and damage evolution during cyclic tests. (a) TRIP evolution; (b) functional and structural damage evolution; (c) D_c evolution.
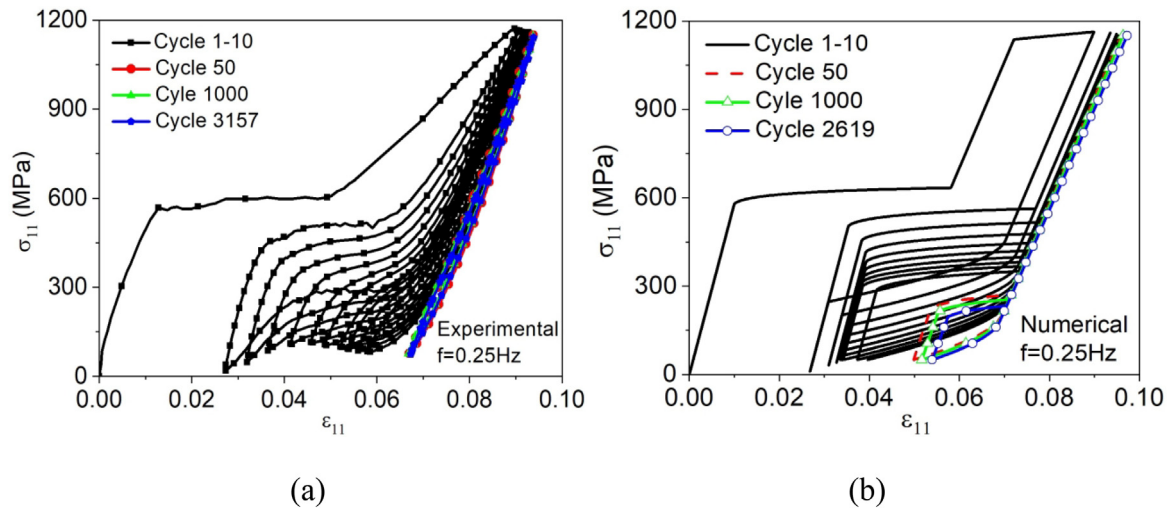

(a)

(b)

Fig. 14. Pseudoelastic behavior for the NiTi SMA wires during fatigue tests, $\sigma_{max} = 1150$ MPa, 0.25 Hz. (a) experimental result; (b) numerical result.

$$\pi = \left\{ \beta^m \,\middle|\, 0 \leq \beta^m \leq 1 (m = +, -, A); \beta^+ + \beta^- + \beta^A \leq 1 \right\} \quad (29)$$

Another constraint is defined by $\kappa_\chi = \kappa_\chi \left(\dot{\beta}^+, \dot{\beta}^-, \dot{\beta}^A \right)$ that represents the phase transformation constraints, that define the conditions for internal sub-loops due to incomplete phase transformations related to the convex set χ (defined for mechanical loadings and thermal loadings from its subsets).

Phase transformations governed by mechanical loadings, $\dot{\Gamma}^\sigma \neq 0$:

$$\chi = \left\{ \dot{\beta}^n \,\middle|\, \begin{array}{l} \dot{\Gamma} \dot{\beta}^+ \geq 0; \dot{\Gamma} \dot{\beta}^A \leq 0 \text{ if } \Gamma_0 > 0 \\ \dot{\Gamma} \dot{\beta}^- \leq 0; \dot{\Gamma} \dot{\beta}^A \geq 0 \text{ if } \Gamma_0 < 0 \end{array} \right\} \quad (30)$$

Phase transformations governed by thermal loadings, $\dot{\Gamma}^\sigma = 0$ (subsets χ_1, χ_2, χ_3):

$$\chi_1 = \left\{ \dot{\beta}^n \,\middle|\, \dot{T} \dot{\beta}^A \geq 0 \right\} \quad (31)$$

$$\chi_2 = \left\{ \dot{\beta}^n \,\middle|\, \dot{T} \dot{\beta}^+ = 0 \,\middle|\, \begin{array}{l} \text{if } \dot{T} > 0, \dot{\beta}^+ > 0 \text{ and } \beta_s^+ \neq 0 \\ \text{if } \dot{T} > 0, \beta^+ \neq \beta_s^+ \text{ and } \beta_s^+ = 0 \\ \text{if } \dot{T} > 0, \dot{\beta}^A = 0 \\ \text{if } \dot{T} < 0, \Gamma^\sigma = 0 \text{ and } \beta^+ \neq \beta_s^+ \end{array} \right\} \quad (32)$$

$$\chi_3 = \left\{ \dot{\beta}^n \,\middle|\, \dot{T} \dot{\beta}^- = 0 \,\middle|\, \begin{array}{l} \text{if } \dot{T} > 0, \dot{\beta}^- > 0 \text{ and } \beta_s^- \neq 0 \\ \text{if } \dot{T} > 0, \beta^- \neq \beta_s^- \text{ and } \beta_s^- = 0 \\ \text{if } \dot{T} > 0, \dot{\beta}^A = 0 \\ \text{if } \dot{T} < 0 \, \Gamma^\sigma = 0 \text{ and } \beta^- \neq \beta_s^- \end{array} \right\} \quad (33)$$

where β_s^+ and β_s^- are the values of β^+ and β^-, respectively, when the phase transformation begins.

4. Numerical simulations

Numerical simulations are now carried out in order to show model capabilities to describe the thermomechanical fatigue of SMAs. The influence of functional and structural fatigue on the thermomechanical behavior of SMAs is of special interest. In this regard, comparisons between numerical and experimental results are presented to verify the proposed modeling. Experimental results presented in Section 2.3 are explored as a reference for the model verification. In all figures related to the numerical-experimental comparisons presented throughout this Section, results containing all numerical cycles are presented in the background, in grayscale, to facilitate the visualization of the strain evolution presented by the material over the cycles. Parameters presented in Table 2 are employed in all simulations and their
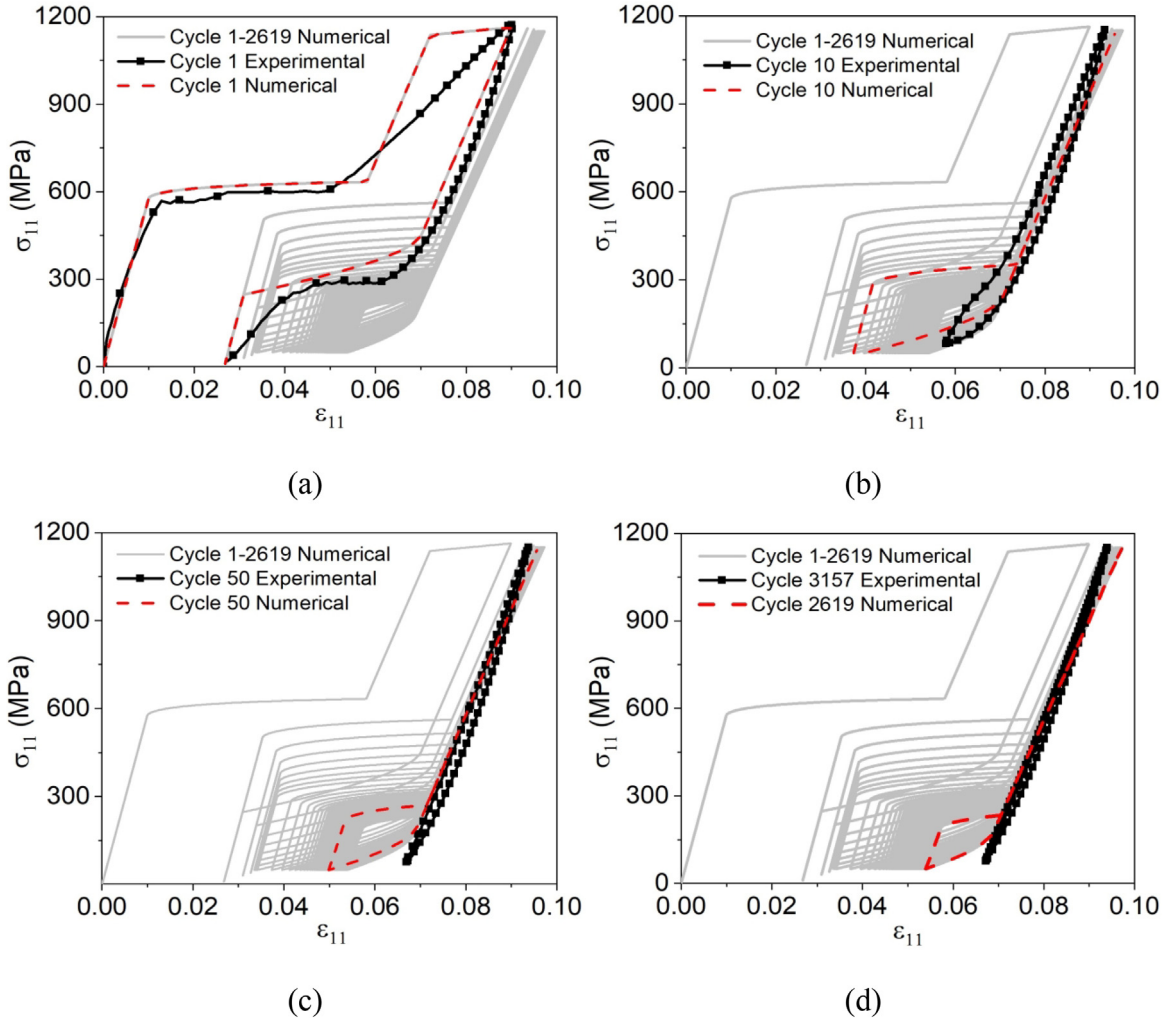

(a)

(b)

(c)

(d)

Fig. 15. Pseudoelastic behavior for the NiTi SMA wires during fatigue tests, $\sigma_{max} = 1150$ MPa, 0.25 Hz. Numerical-experimental comparative for different cycles: (a) cycle 1; (b) cycle 10; (c) cycle 50; (d) cycles 3157 (experimental) and 2619 (numerical).

choices are based on experimental measurements discussed in Section 2, and on the optimization to match experimental data. Sensitivity and uncertainty analyses for one-dimensional media are discussed in Oliveira et al. (2014).

Initially, a loading process within the yield surface is treated. For this purpose, consider the experimental test where the pseudoelastic NiTi SMA wire is subjected to cyclic tension with peak stress of 750 MPa (load region: I, II, III) with a frequency of 0.25 Hz, shown in Fig. 9 (a). Fig. 9 (b) presents numerical simulations of the same test, showing a good agreement with experimental data. The same aspects related with functional damage, directly related to TRIP, and the same prediction of the failure cycle should be observed and will be discussed with more details in the sequence.

Fig. 10 presents the numerical-experimental comparison considering four different cycles:1, 10, 50, and the last cycle before failure obtained experimentally (2308) and the last cycle predicted by the proposed model (2284). Note that the material undergoes a loss of actuation with the increase of the number of cycles due to the transformation induced plasticity and the accumulation of functional and structural damage. Fig. 11 shows the evolution of volume fractions for the analyzed cycles. During the first cycles, the material has 100% of its performance capacity. With the evolution of damage, this percentage gradually decreases until reaching approximately 60% in the last cycle before the failure, as shown in

Fig. 11 (d). Fig. 12 shows numerical-experimental comparison of phase transformation critical stresses, σ^{M_s} and σ^{A_s}. It is noticeable that the loss of functionality caused by the accumulation of damage promotes a significant reduction in phase transformation critical stresses, which assume similar values in the last cycles before the rupture. In general, it should be pointed out the good agreement between numerical and experimental results presented in Fig. 10 and Fig. 12, showing the model capability to describe the evolution of material response during fatigue tests.

The evolution of TRIP strain and damage is presented in Fig. 13. Fig. 13 (a) presents the evolution of TRIP showing that the material undergoes a rapid stabilization when TRIP reaches a constant value, around 10 cycles. Fig. 13 (b) presents the evolution of functional and structural damage. After 2284 cycles, the functional damage reaches a value of approximately 12% promoting the reduction of the functional properties of the material. On the other hand, the structural damage follows a trend of linear evolution reaching approximately 2% in the last cycle before the failure. Fig. 13 (c) shows the evolution of D_c over the cycles until reaching $D_c^{crit} = 0.16$.

Concerning classical plasticity, consider the experimental test of the cyclic pseudoelastic behavior presented in Fig. 14 (a). Basically, the loading process reaches the yield surface, assuming a peak stress of 1150 MPa (load region: I, II, III, IV), at a frequency of 0.25 Hz. Fig. 14 (b) presents numerical results showing the same
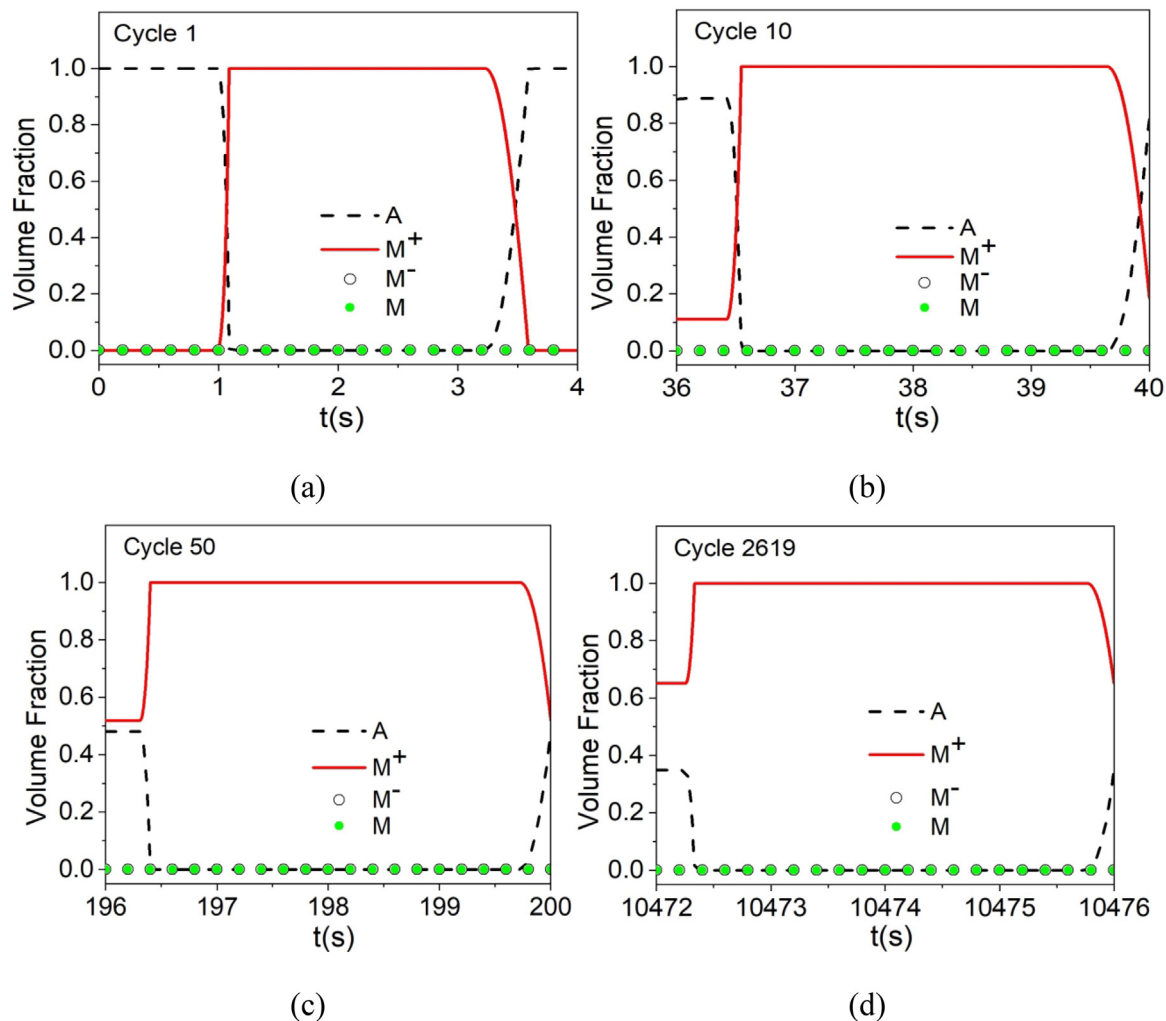

Fig. 16. Evolution of volume fractions through different cycles to evaluate functional and structural fatigue. (a) cycle 1; (b) cycle 10; (c) cycle 50; (d) cycle 2619.

characteristics related to all involved phenomena: phase transformation, transformation induced plasticity, classical plasticity and fatigue. The material failure, predicted by the proposed model, occurs with 2619 cycles, representing a variation of approximately 17% concerning the experimental result.

Fig. 15 shows the numerical-experimental comparison considering different cycles: 1, 10, 50, 3157 (experimental result) and 2619 (numerical result). Fig. 16 shows the evolution of volume fractions for the analyzed cycles. It is noticeable that classic plasticity together with TRIP promotes a rapid loss of performance during
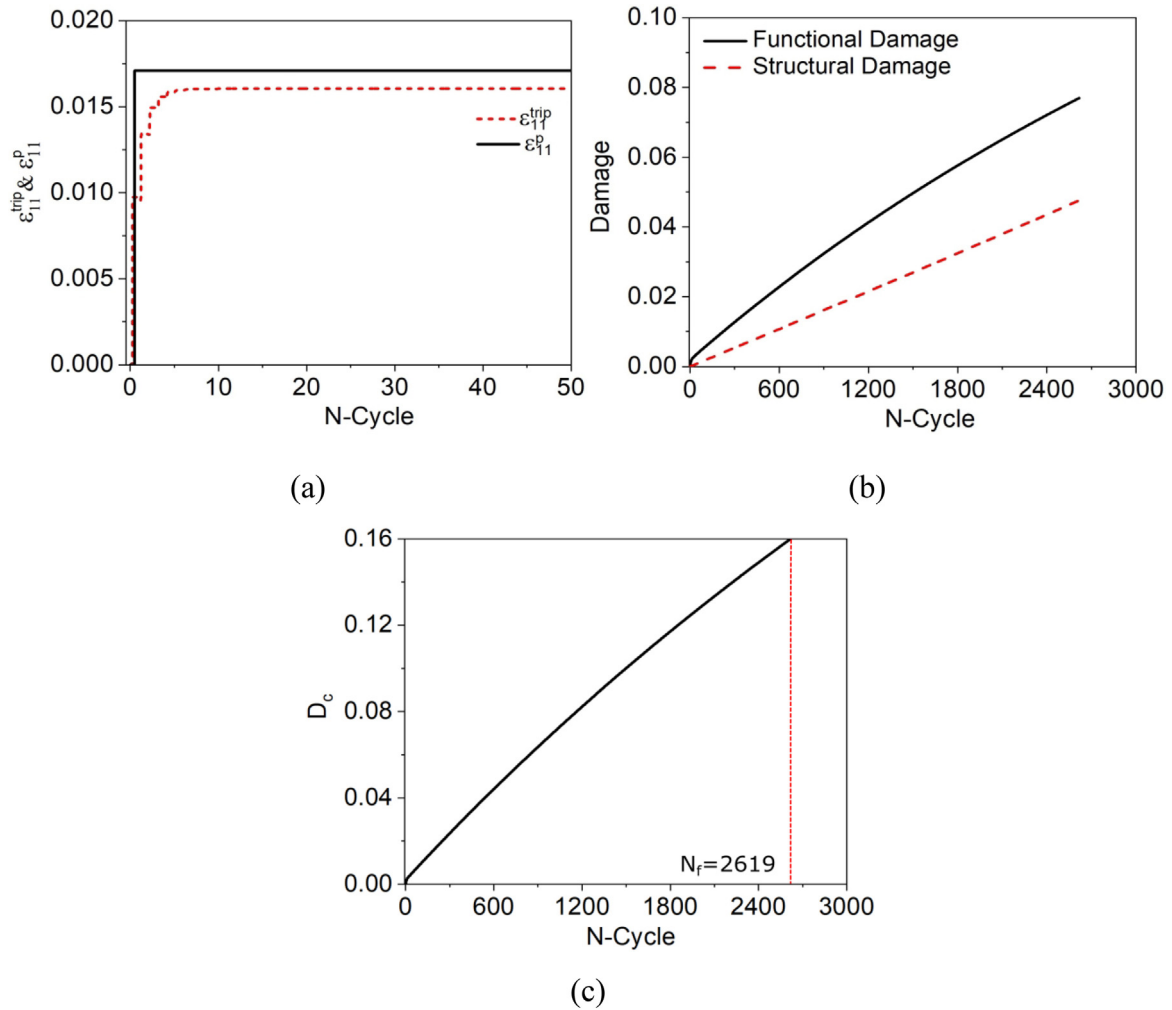

(a)

(b)

(c)

Fig. 17. Plastic strain, TRIP, and damage evolution during cyclic tests. (a) plastic strain and TRIP evolution; (b) functional and structural damage evolution; (c) D_c evolution.
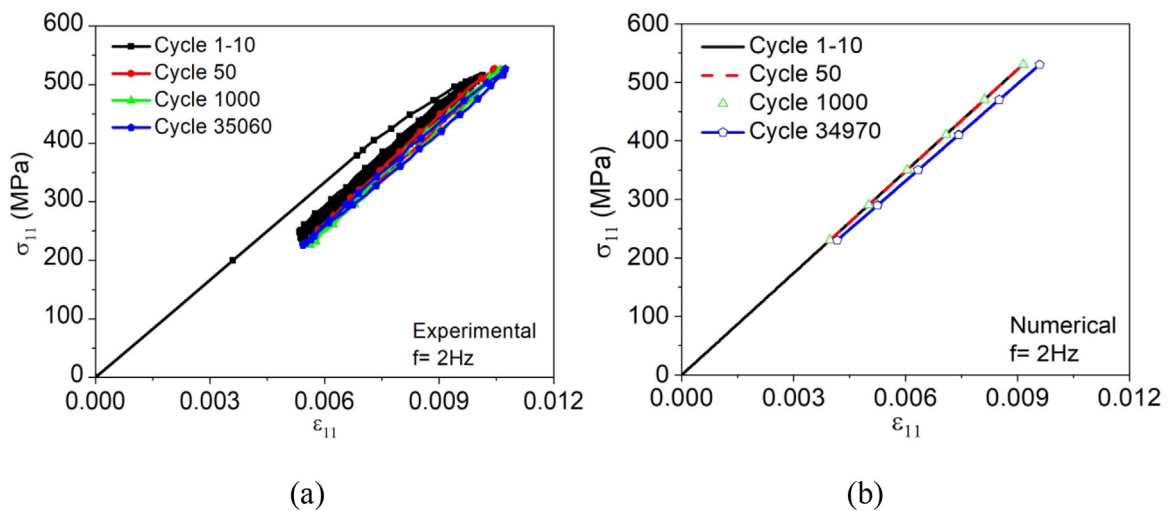

(a)

(b)

Fig. 18. Pseudoelastic behavior for the NiTi SMA wires during fatigue tests, $\sigma_{max} = 530$ MPa, 2 Hz. (a) experimental result; (b) numerical result.

the first cycles, of approximately 50%, as shown in Fig. 16 (c). Nevertheless, after the loss of performance, SMA has not completely lost its phase transformation capacity. After this stage, the material loses its phase transformation capacity due to the damage evolu-

tion, remaining approximately 35% in the last cycle, as can be seen in Fig. 16 (d).

Fig. 17 (a) shows the evolution of plastic strain and TRIP strain. Similar to the previous test, it is observed that the material under-
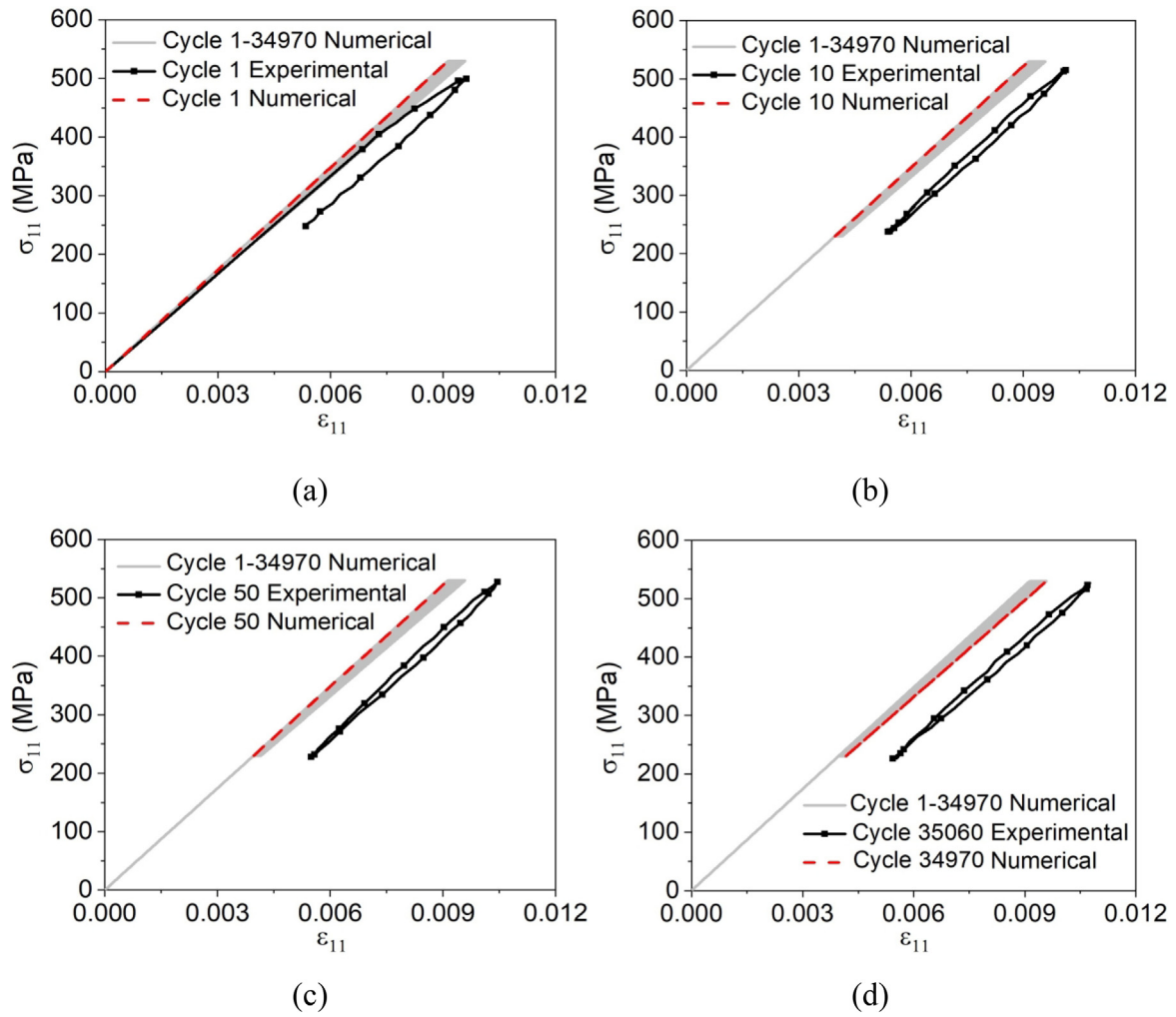

Fig. 19. Pseudoelastic behavior for the NiTi SMA wires during fatigue tests, $\sigma_{max} = 530$ MPa, 2 Hz. Numerical-experimental comparative for different cycles: (a) cycle 1; (b) cycle 10; (c) cycle 50; (d) cycles 35,060 (experimental) and 34,970 (numerical).
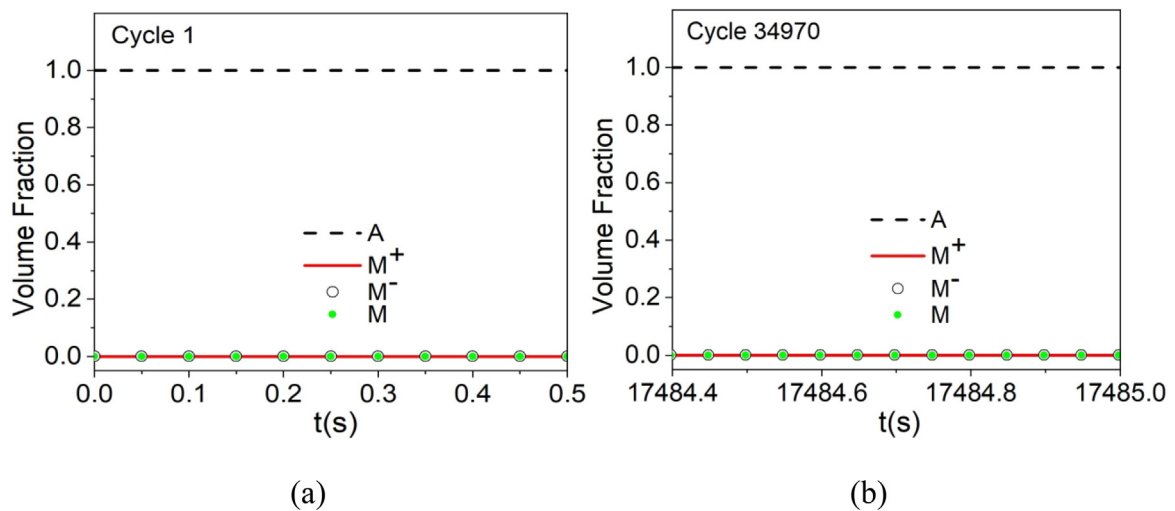

Fig. 20. Evolution of volume fractions through different cycles to evaluate functional and structural fatigue. (a) cycle 1; (b) cycle 34970.

goes a rapid stabilization, where plastic strain and TRIP reaches a constant value after a few loading cycles. Fig. 17 (b) shows the evolution of functional and structural damage. Note that the functional damage has an evolution similar to the one observed previously, however, the loss of performance caused by plasticity during the initial cycles reduces the rate of evolution of functional damage by approximately 50% when compared to the previous test. Once again, the structural damage follows a trend of linear evolution reaching approximately 5% in the last cycle before the predicted failure. Finally, Fig. 17 (c) shows the evolution of D_c until reaching $D_c^{crit} = 0.16$.

SMA fatigue tests related to elastic responses, without phase transformations, are presented in the sequence. The first test considers the elastic cyclic loading in the austenitic phase, varying between 230 and 530 MPa (load region: I) at a frequency of 2 Hz, as shown in Fig. 18 (a). Fig. 18 (b) shows numerical simulations of the same test. Fig. 19 shows a comparison between numerical and experimental results for different cycles: 1, 10, 50, 35,060 (experimental result) and 34,970 (numerical result predicted by the model). TRIP effect and functional damage are not present since

there is no phase transformation. Results addressed in Fig. 19 show that in the absence of phase transformation, the maximum strain presented over the cycles is around 1%. Therefore, the changes observed in the response of the material can be essentially associated with the evolution of structural damage. Fig. 20 presents the evolution of volume fractions for the first and last cycle confirming that response is restricted to the austenitic phase. Fig. 21 (a) presents the evolution of functional and structural damage. The functional damage remains constant and equal to zero during all loading process. On the other hand, structural damage reaches a value of approximately 5% in the last cycle. Fig. 21 (b) shows the evolution of D_c. It should be highlighted that the model represents the thermomechanical behavior of the SMAs subjected to loads where phase transformations do not occur, presenting a fatigue failure estimation coherent with experimental data.

The next test aims to evaluate the evolution of structural damage due to elastic response in the martensitic phase (load region: III). A training procedure with peak stress of 900 MPa and a frequency of 1 Hz, followed by a cyclic loading within the martensitic elastic region at a frequency of 2 Hz. Therefore, the accumulation of
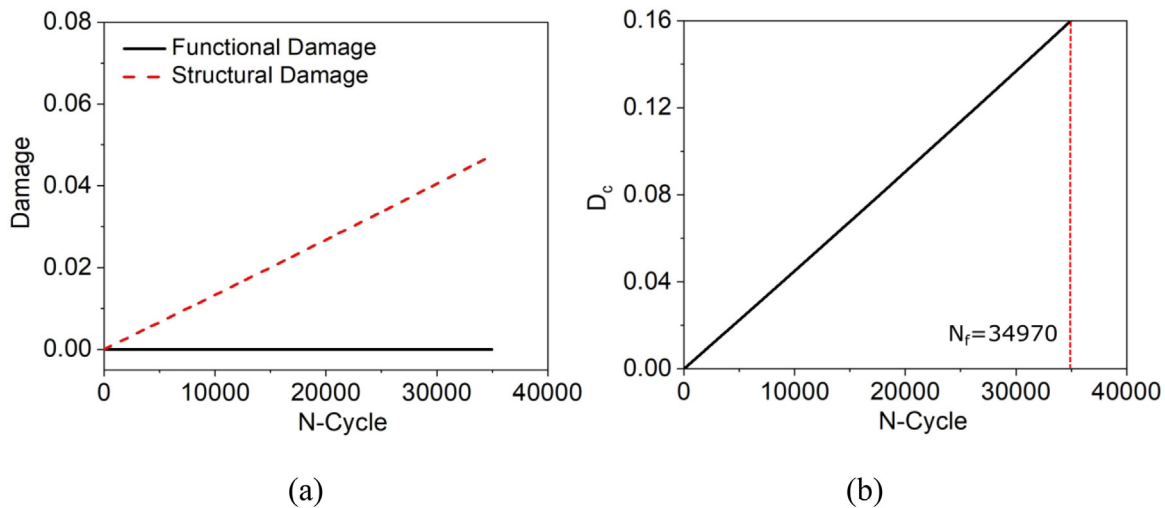

Fig. 21. Damage evolution during cyclic tests. (a) functional and structural damage evolution; (b) D_c evolution.
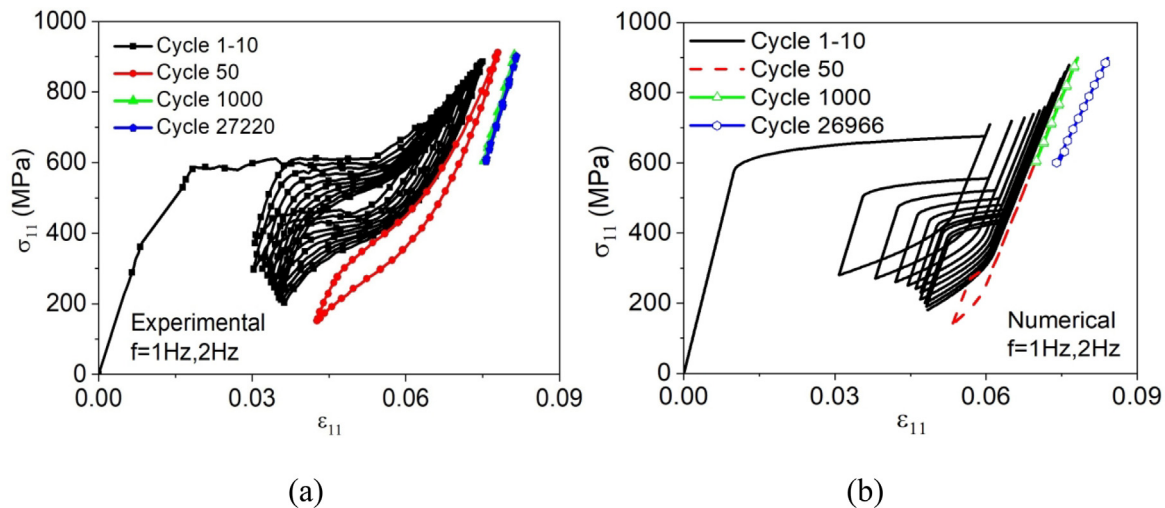

Fig. 22. Pseudoelastic behavior for the NiTi SMA wires during fatigue tests, $\sigma_{max} = 900$ MPa, 1, 2 Hz. (a) experimental result; (b) numerical result.

functional damage occurs only during the first 50 cycles, remaining constant afterward. Fig. 22 (a) shows the experimental result, while Fig. 22 (b) presents numerical simulations obtained from the proposed model.

Fig. 23 shows the numerical-experimental comparison for cycles 1, 10, 50, 27,220 (experimental result), and 26,966 (numerical result predicted by the model). After the training process, an evolution of residual strain is observed within the martensitic elastic region, due to the evolution of structural damage. In general, the model is capable to capture the main aspects of functional and structural fatigue, being in close agreement with experimental tests.

Fig. 24 shows the evolution of volume fractions showing that phase transformations occur only before the 50th cycle and, afterward, a martensitic elastic response is observed, without phase transformations. Besides, due to loading applied, it is observed that the inverse transformation during the first cycles does not occur completely, affecting the hysteresis loop and causing a significant reduction of the volume fractions through the cycles.

Fig. 25 (a) presents the evolution of TRIP strain during the first 50 cycles showing that the material undergoes a rapid stabilization, where TRIP strain reaches a constant value, around 20 cycles. Fig. 25 (b) presents the evolution of functional and structural damage during cyclic loading process showing that, after 50th cycle,

the functional damage stabilizes while the structural damage increases linearly up to a maximum value of approximately 18% in the last cycle before failure. Fig. 25 (c) shows the evolution of D_c over the cycles until reaching $D_c^{crit} = 0.16$.

Table 3 shows the comparison of experimental fatigue lifetime and predicted by the proposed model. It should be pointed out a good fatigue life prediction of SMAs subjected to different loading conditions.

From the simulations presented, it is concluded that the model shows the ability to capture the general thermomechanical behavior associated with SMAs taking into account the classical plasticity, TRIP effect, functional and structural fatigue during cyclic loadings, showing a good agreement with experimental data.

4.1. Influence of structural damage on the loss of actuation performance

In order to evaluate the influence of structural damage on the loss of actuation of SMA functional properties, a numerical simulation is presented establishing a comparison between the complete model (CM), with structural and functional damage, and the model considering only functional damage (FFM). A loading process with peak stress of 750 MPa and a frequency of 0.25 Hz is employed.
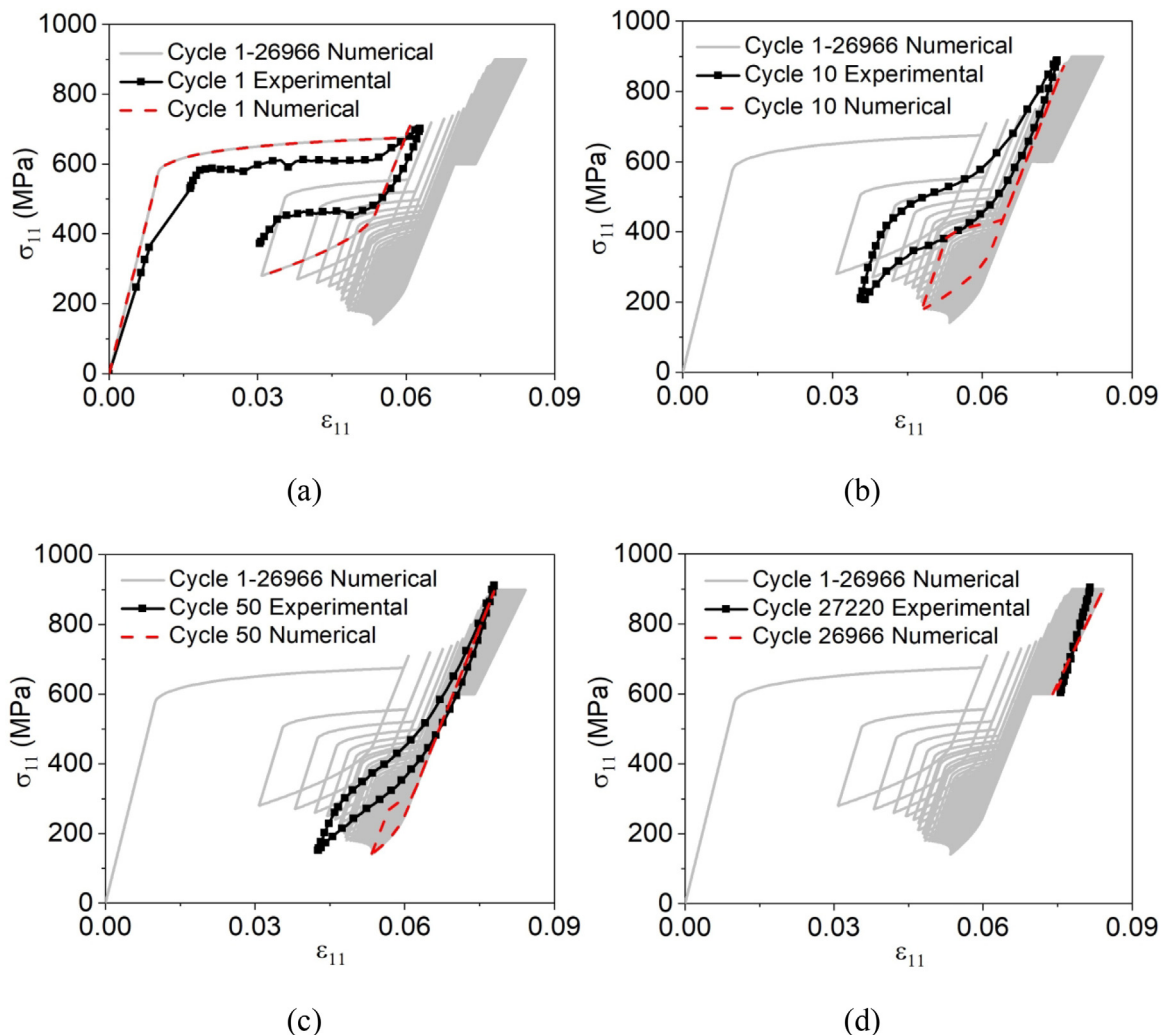

(a)

(b)

(c)

(d)

Fig. 23. Pseudoelastic behavior for the NiTi SMA wires during fatigue tests, $\sigma_{max} = 900$ MPa, 1, 2 Hz. Numerical-experimental comparative for different cycles: (a) cycle 1; (b) cycle 10; (c) cycle 50; (d) cycles 27,220 (experimental) and 26,966 (numerical).
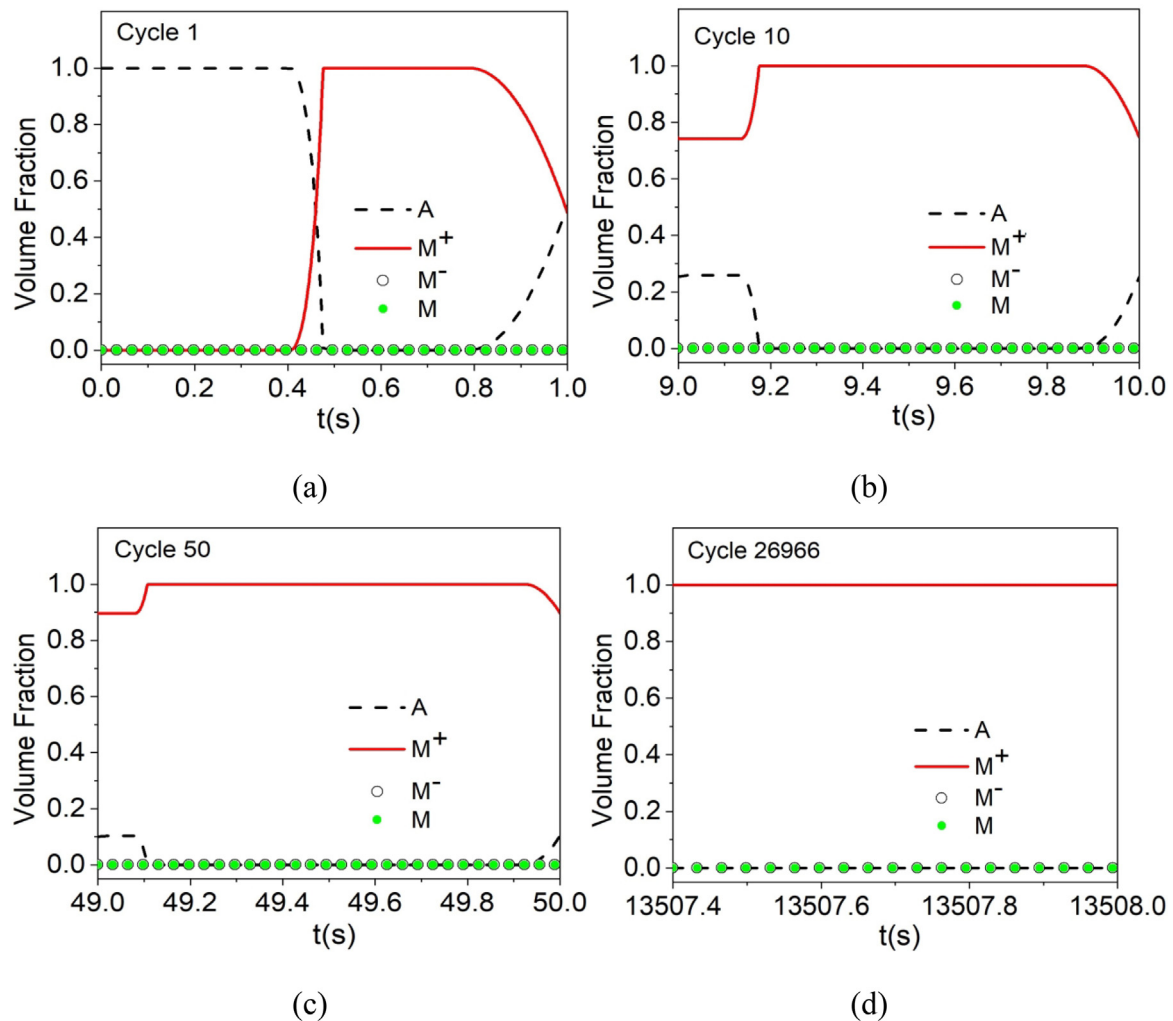
Fig. 24. Evolution of volume fractions through different cycles to evaluate functional and structural fatigue. (a) cycle 1; (b) cycle 10; (c) cycle 50; (d) cycle 26966.

Fig. 26 presents results showing stress-strain curves for different cycles of the SMA response, volume fractions and damage evolutions. Note that the structural damage evolution changes the thermomechanical behavior of the material modifying its functional characteristics. Nevertheless, the actuation performance is not significantly affected due to the structural damage as can be seen in Fig. 26 (c) that shows the volume fraction evolutions for cycle 2284. In this regard, it is concluded that the structural damage acts together with the functional damage to promote the loss of functionality, but the functional damage is preponderant to define the functional properties.

5. Conclusions

The present contribution proposes a three-dimensional constitutive model to describe thermomechanical behavior of shape memory alloys including structural and functional fatigue. The model is developed within the framework of generalized standard materials formalism. Local continuum damage is employed to describe structural and functional damage. A novel equivalent crit-

ical damage is proposed in order to define the fatigue life considering different behaviors of martensitic and austenitic phases. The main macroscopic characteristics presented by pseudoelastic SMAs subjected to fatigue tests are analyzed through experimental approach. Experimental results allow one to verify the influence of the stress levels and frequency on the SMA functional properties. Four kinds of results are treated: the first one considers a loading process within the yield surface in order to analyze the influence of TRIP, functional and structural damage. The second one considers a loading process that reaches the yield surface evaluating the effect of plasticity on the fatigue life. The two other tests are performed without phase transformations estimating the influence of structural damage on the response of the material. Numerical simulations are carried out and compared with experimental data. In general, the model is capable to capture the main features of SMA thermomechanical behavior, including several phenomena. Structural and functional fatigue are represented in close agreement with experimental tests, allowing proper predictions of fatigue life and loss of actuation. A numerical simulation is carried out in order to evaluate the influence of structural damage on the loss of actuation performance. Structural damage acts together with
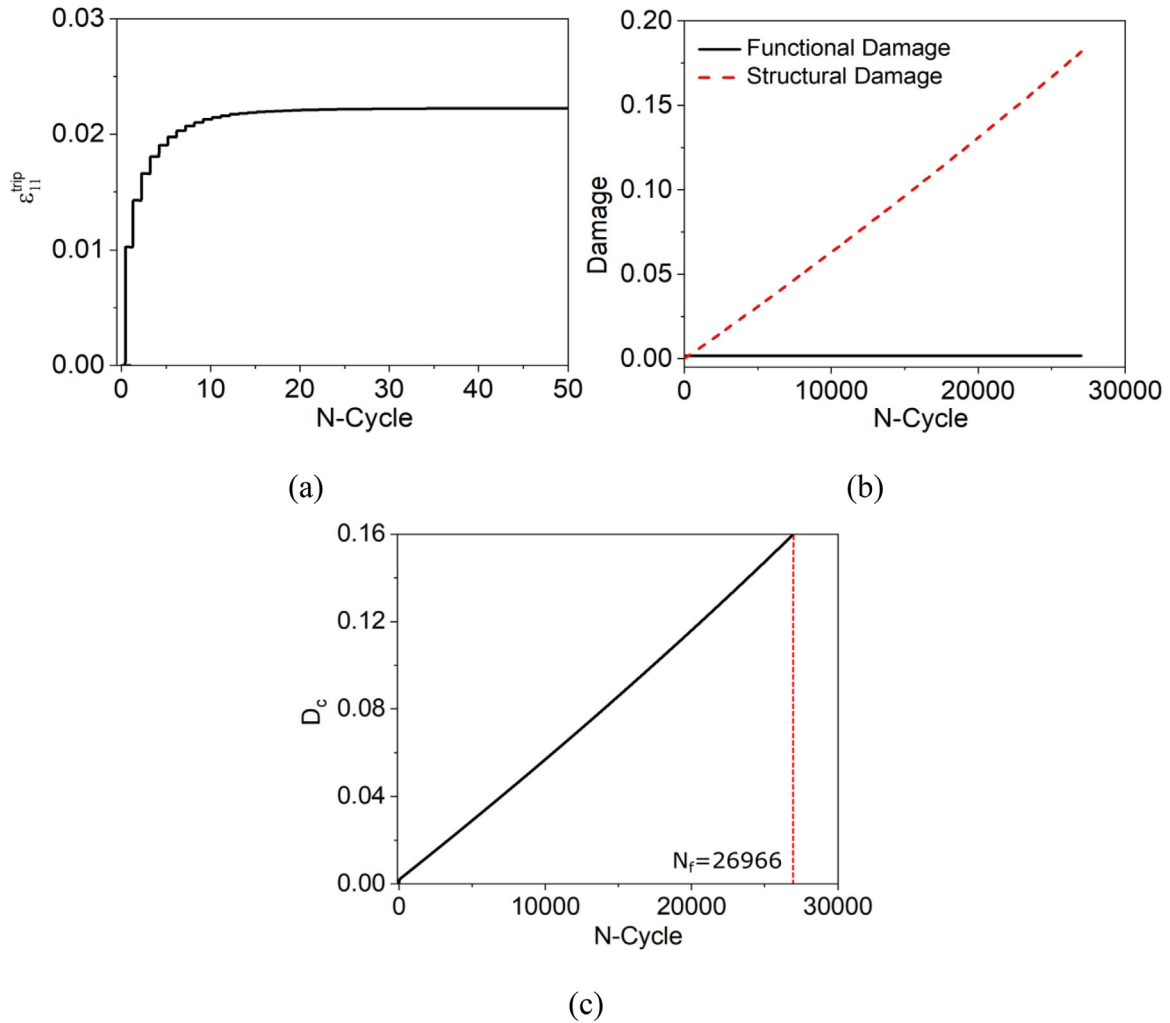
Fig. 25. TRIP strain and damage evolution during cyclic tests. (a) TRIP evolution; (b) functional and structural damage evolution; (c) D_c evolution.

the functional damage promoting the reduction of the SMA functional properties. Nevertheless, the functional damage is preponderant on the loss of functionality.

Declaration of Competing Interest

The authors declare that they have no known competing financial interests or personal relationships that could have appeared to influence the work reported in this paper.

Acknowledgements

Appendix A

This appendix presents a brief discussion about constitutive model parameters. A detailed description can be found in Oliveira et al. (2014), Oliveira et al. (2016), Oliveira et al. (2018); Paiva et al. (2005), and Dornelas et al. (2020).

The phase transformation parameter α^h_{ijkl} is a fourth-order tensor that controls the stress-strain hysteresis loop width. Due to

symmetry assumptions, α^h_{ijkl} can be represented by a matrix considering the parameters α^h_N and α^h_S, related to normal and shear behaviors respectively, similar to the isotropic elastic tensor.

$$\alpha^h_{ijkl} \equiv \begin{bmatrix} \alpha^h_N & \alpha^h_N - \alpha^h_S & \alpha^h_N - \alpha^h_S & 0 & 0 & 0 \\ \alpha^h_N - \alpha^h_S & \alpha^h_N & \alpha^h_N - \alpha^h_S & 0 & 0 & 0 \\ \alpha^h_N - \alpha^h_S & \alpha^h_N - \alpha^h_S & \alpha^h_N & 0 & 0 & 0 \\ 0 & 0 & 0 & \alpha^h_S & 0 & 0 \\ 0 & 0 & 0 & 0 & \alpha^h_S & 0 \\ 0 & 0 & 0 & 0 & 0 & \alpha^h_S \end{bmatrix} \quad (A.1)$$

Besides, r_{kl} is a symmetric second-order tensor associated with the loading history.

$$r_{kl} = \begin{cases} +1, \; if \; \sigma_{kl} > 0 \\ 0, \; if \; \sigma_{kl} = 0 \\ -1, \; if \; \sigma_{kl} < 0 \end{cases} \quad (A.2)$$

On situations where mechanical loadings are obtained through non-simultaneous, multiaxial loadings, the r_{kl} is calculated for the subsequent loadings (assuming stress driving cases), as shown below:

$$r_{kl} = \frac{\sigma_{kl}}{|S^{max}_{kl}|} \; if \; \beta^+ \neq 0 \, or \, \beta^- \neq 0 \quad (A.3)$$
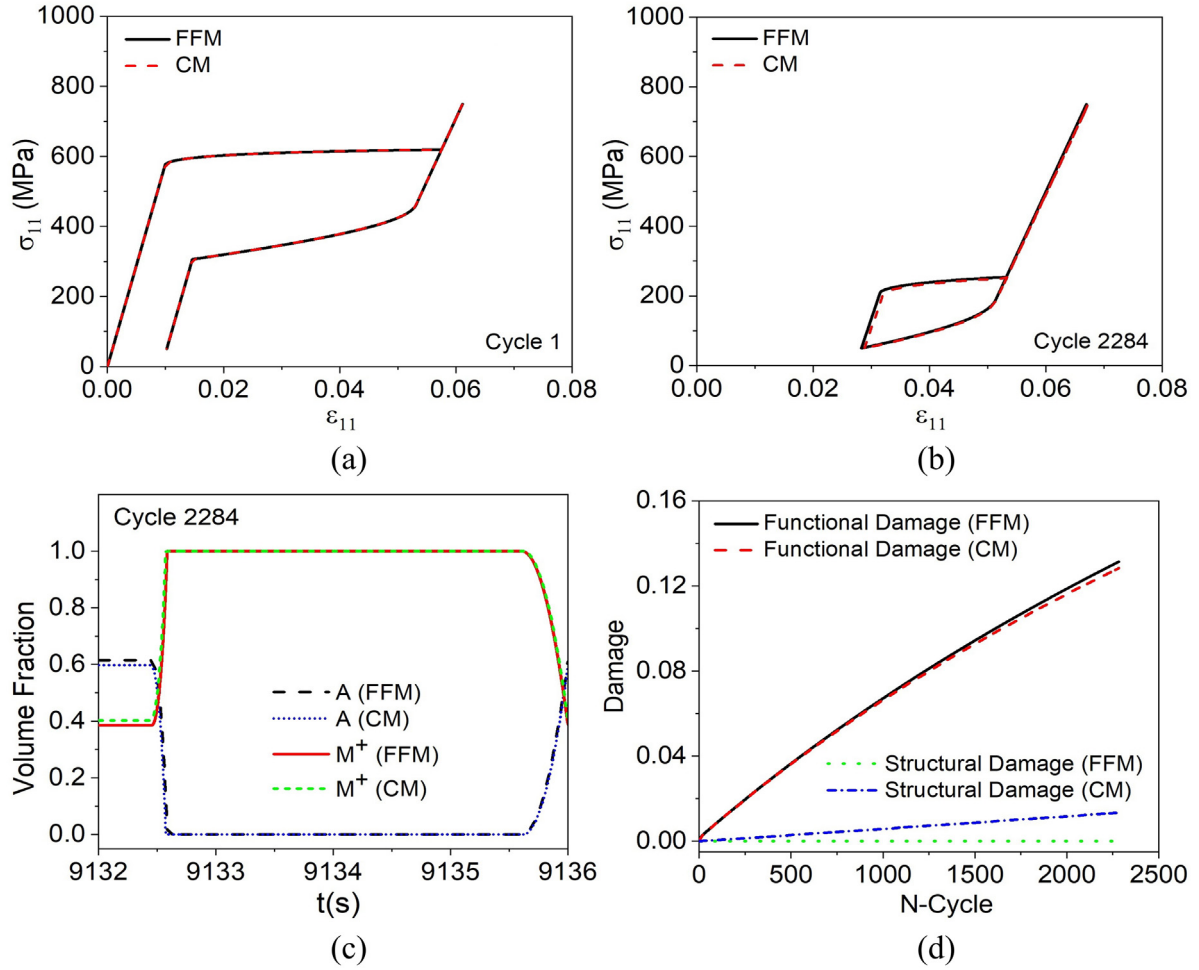
Fig. 26. Comparison between numerical results obtained considering only functional damage (FFM) and considering functional and structural damage on the analysis (CM). (a) cycle 1; (b) cycle 2284; (c) volume fraction evolution for cycle 2284; (d) functional and structural damage evolution.

Table 3
Comparison between experimental results and predicted by the proposed model.

	Frequency (Hz)	σ_{max}(MPa)	N_f(experimental)	N_f(predicted)	Variation (%)
Pseudoelastic	0.25	750	2308	2284	1.0
Pseudoelastic - plasticity	0.25	1150	3157	2619	17.0
Elastic - austenitic phase	2	530	35,060	34,970	0.3
Elastic - martensitic phase	1, 2	900	27,220	26,966	0.9

where S_{kl}^{max} is the maximum value of the mechanical loading that can be a stress or a strain. Additionally, note that $\frac{\sigma_{kl}}{|S_{kl}^{max}|} = 0$ if $S_{kl}^{max} = 0$.

The internal dissipation during the phase transformation can be defined taking into account different characteristics of the phase transformation kinetics during loading and unloading processes. Thus, different values can be associated with the parameters η^+, η^- and η^A:

$$\begin{cases} \eta^\pm = \eta_L^\pm \text{ if } \dot{\Gamma} > 0 \\ \eta^\pm = \eta_U^\pm \text{ if } \dot{\Gamma} < 0 \end{cases}, \begin{cases} \eta^A = \eta_L^A \text{ if } \dot{\Gamma} > 0 \\ \eta^A = \eta_U^A \text{ if } \dot{\Gamma} < 0 \end{cases} \quad (A.4)$$

The parameters $\eta_L^+, \eta_L^-, \eta_U^+, \eta_U^-, \eta_L^A$ and η_U^A are calculated considering fourth-order tensors, assuming the isotropy of the material. For this purpose, consider a general formulation defined from the symbol $\mathcal{N}$ that represents each of the previous parameters, as follows:

$$\begin{cases} (\mathcal{N}) = r_{ij}(\widetilde{\mathcal{N}})_{ijkl}r_{kl} \text{ if } \Gamma^\sigma \neq 0 \\ (\mathcal{N}) = (\mathcal{N})_N \text{otherwise} \end{cases} \quad (A.5)$$

where $(\widetilde{\mathcal{N}})_{ijkl}$ is given by:

$$(\widetilde{\mathcal{N}})_{ijkl} \equiv \begin{bmatrix} (\mathcal{N})_N & (\mathcal{N})_N - (\mathcal{N})_S & (\mathcal{N})_N - (\mathcal{N})_S & 0 & 0 & 0 \\ (\mathcal{N})_N - (\mathcal{N})_S & (\mathcal{N})_N & (\mathcal{N})_N - (\mathcal{N})_S & 0 & 0 & 0 \\ (\mathcal{N})_N - (\mathcal{N})_S & (\mathcal{N})_N - (\mathcal{N})_S & (\mathcal{N})_N & 0 & 0 & 0 \\ 0 & 0 & 0 & 2(\mathcal{N})_S & 0 & 0 \\ 0 & 0 & 0 & 0 & 2(\mathcal{N})_S & 0 \\ 0 & 0 & 0 & 0 & 0 & 2(\mathcal{N})_S \end{bmatrix}$$

(A.6)

where $(\mathcal{N})_N$ and $(\mathcal{N})_S$ represents normal and shear components of the specific parameter, respectively.

Concerning classical plasticity parameters, K is plastic modulus; H is the kinematic hardening modulus. These parameters are defined considering a rule of mixture: $K = K^M + \beta^A (K^A - K^M)$ and $\frac{1}{H} = \frac{1}{H^M} + \beta^A \left(\frac{1}{H^A} - \frac{1}{H^M} \right)$, similar to the presented previously for E_{ijkl} and Ω_{ij}. In addition, η^I defines the coupling between phase transformation and isotropic hardening. The coupling between phase transformation and kinematic hardening is defined by the second-order tensor, as follows:

$$\eta^K_{ij} \equiv \eta^K \begin{bmatrix} 1 & 1 & 1 \\ 1 & 1 & 1 \\ 1 & 1 & 1 \end{bmatrix}$$

(A.7)

The yield surface is defined by the yield stress σ_Y that has different values for austenitic and martensitic phases. Their values are also temperature dependent and the following macroscopic adjustment is employed:

$$\begin{cases} \sigma_Y = \sigma_Y^M & \text{if } T \leq T^M \\ \sigma_Y = \frac{\sigma_Y^M (T^A - T) + \sigma_Y^{Ai} (T - T^M)}{T^A - T^M} & \text{if } T^M < T \leq T^A \\ \sigma_Y = \frac{\sigma_Y^{Ai} (T^F - T) + \sigma_Y^{Af} (T - T^A)}{T^F - T^A} & \text{if } T^M < T \leq T^F \end{cases}$$

(A.8)

where T^A is the temperature above which the austenitic phase is stable; T^F is a reference temperature for the determination of the yield stress for high temperatures; σ_Y^M is yield stress of the martensitic phase; σ_Y^{Ai} and σ_Y^{Af} define the thermal variation of the yield stress of the austenitic phase.

TRIP effect is described by the parameters $M_{13}, M_{31}, M_{23}, M_{32}, M_{34}$ and M_{43}. These parameters have a saturation characteristic defined from TRIP variables: $M_{ij} = \widehat{M}_{ij} \exp\left(-m^M \xi^i \right)$, where m^M is a saturation parameter. To control the amount of TRIP strain at different temperatures, the following expressions are defined:

$$\widehat{M}_{ij} = \begin{cases} 0 & \text{if } T < T^{trip} \\ \widehat{M}_{ij}^R \frac{(T - T^{trip})}{(T^F - T^{trip})} & \text{if } T \geq T^{trip} \end{cases}$$

(A.9)

where $\widehat{M}_{ij}^R$ is a reference value of $\widehat{M}_{ij}$ at $T = T^{trip}$ and T^{trip} is a temperature below which TRIP should not occur.

In addition, other parameters as $\alpha, L_o^+, L_o^-, L_o^A, L^+, L^-, L^A$, also presents a saturation characteristic as follows:

$$( ) = \widehat{( )} \left[\frac{n + \exp(-m^{( )} \xi^{\pm})}{n + 1} \right]$$

(A.10)

where n is used to obtain an appropriate adjustment and $m^{( )}$ is a saturation parameter.

References

ASTM F2063–18. Standard Specification for Wrought Nickel-Titanium Shape Memory Alloys for Medical Devices and Surgical Implants. ASTM International West, Conshohocken, PA, 2018..

ASTM F2516-14. Standard Test Method for Tension Testing of Nickel-Titanium Superelastic Materials. ASTM International, West Conshohocken, PA, 2014..

Barbarino, S, Saavedra Flores, E I, Ajaj, R M, Dayyani, I, Friswell, M I, 2014. A review on shape memory alloys with applications to morphing aircraft. Smart Mater. Struct. 23 (6), 063001. https://doi.org/10.1088/0964-1726/23/6/063001.

Barrera, Noemi, Biscari, Paolo, Urbano, Marco Fabrizio, 2014. Macroscopic modeling of functional fatigue in shape memory alloys. Eur. J. Mech. A. Solids 45, 101–109.

Chatziathanasiou, Dimitris, Chemisky, Yves, Chatzigeorgiou, George, Meraghni, Fodil, 2016. Modeling of coupled phase transformation and reorientation in shape memory alloys under non-proportional thermomechanical loading. Int. J. Plast. 82, 192–224.

Chemisky, Yves, Hartl, Darren J., Meraghni, Fodil, 2018. Three-dimensional constitutive model for structural and functional fatigue of shape memory alloy actuators. Int. J. Fatigue 112, 263–278.

Cisse, Cheikh, Zaki, Wael, Zineb, Tarak Ben, 2016. A review of modeling techniques for advanced effects in shape memory alloy behavior. Smart Mater. Struct. 25 (10), 103001. https://doi.org/10.1088/0964-1726/25/10/103001.

Dornelas, V.M., Oliveira, S.A., Savi, M.A., 2020. A macroscopic description of shape memory alloy functional fatigue. Int. J. Mech. Sci. 170, 105345.

Eggeler, G., Hornbogen, E., Yawny, A., Heckmann, A., Wagner, M., 2004. Structural and functional fatigue of NiTi shape memory alloys. Mater. Sci. Eng., A 378 (1-2), 24–33.

Figueiredo, A, Modenesi, P, Buono, V, 2009. Low-cycle fatigue life of superelastic NiTi wires. Int. J. Fatigue 31 (4), 751–758.

Halphen, B., Nguyen, Q.S., 1975. Sur les Matériaux Standard Généralisés. Journal de Mécanique 14, 39–63.

Hartl, D.J., Chemisky, Y., Meraghni, F., 2014. Three-dimensional constitutive model considering transformation-induced damage and resulting fatigue failure in shape memory alloys. Proc.SPIE 9058, 905805.

Mohd Jani, Jaronie, Leary, Martin, Subic, Aleksandar, Gibson, Mark A., 2014. A review of shape memory alloy research, applications and opportunities. Materials & Design (1980-2015) 56, 1078–1113.

Jaureguizahar S.M., Chapetti M.D., Yawny A. Fatigue of NiTi shape memory wires. 21st European Conference on Fracture, ECF21, 20-24 June 2016, Catania, Italy, 2016..

Jaureguizahar, S.M., Chapetti, M.D., Yawny, A., 2018. A novel experimental method to assess the fatigue behavior of pseudoelastic NiTi wires. Int. J. Fatigue 116, 300–305.

Kang, Guozheng, Kan, Qianhua, Yu, Chao, Song, Di, Liu, Yujie, 2012. Whole-life transformation ratchetting and fatigue of super-elastic NiTi Alloy under uniaxial stress-controlled cyclic loading. Mater. Sci. Eng.: A 535, 228–234.

Kang, Guozheng, Song, Di, 2015. Review on structural fatigue of NiTi shape memory alloys: pure mechanical and thermo-mechanical ones. Theor. Appl. Mech. Lett. 5 (6), 245–254.

Kollerov, Mikhail, Lukina, Elena, Gusev, Dmitriy, Mason, Peter, Wagstaff, Paul, 2013. Impact of material structure on the fatigue behaviour of NiTi leading to a modified Coffin–Manson equation. Mater. Sci. Eng., A 585, 356–362.

Lagoudas, D.C., 2008. Shape memory alloys: modeling and engineering applications. Department of Aerospace Engineering Texas A&M University, Springer Science Business Media, LLC.

Lagoudas, D C, Miller, D A, Rong, L, Kumar, P K, 2009. Thermomechanical fatigue of shape memory alloys. Smart Mater. Struct. 18 (8), 085021. https://doi.org/10.1088/0964-1726/18/8/085021.

Lemaitre, Jean, Chaboche, Jean-Louis (Eds.), 1990. Mechanics of Solid Materials. Cambridge University Press.

Mahtabi, M.J., Shamsaei, Nima, Rutherford, Benjamin, 2015a. Mean strain effects on the fatigue behavior of superelastic nitinol alloys: an experimental investigation. Proc. Eng. 133, 646–654.

Mahtabi, M.J., Shamsaei, Nima, Mitchell, M.R., 2015b. Fatigue of Nitinol: the state-of-the-art and ongoing challenges. J. Mech. Behav. Biomed. Mater. 50, 228–254.

Maletta, C, Sgambitterra, E, Furgiuele, F, Casati, R, Tuissi, A, 2012. Fatigue of pseudoelastic NiTi within the stress-induced transformation regime: a modified Coffin–Manson approach. Smart Mater. Struct. 21 (11), 112001. https://doi.org/10.1088/0964-1726/21/11/112001.

Maletta, C., Sgambitterra, E., Furgiuele, F., Casati, R., Tuissi, A., 2014. Fatigue properties of a pseudoelastic NiTi alloy: strain ratchetting and hysteresis under cyclic tensile loading. Int. J. Fatigue 66, 78–85.

Savi, M A, Pacheco, M P C L, Garcia, M S, Aguiar, R A A, Souza, L F G, da Hora, R B, 2015. Nonlinear Geometric Influence on the Mechanical Behavior of Shape Memory Alloy Helical Spring. Smart Materials and Structures 24 (3), 0350122015. https://doi.org/10.1088/0964-1726/24/3/035012.

Scirè Mammano, G., Dragoni, E., 2014. Functional fatigue of Ni–Ti shape memory wires under various loading conditions. Int. J. Fatigue 69, 71–83.

Monteiro Jr, Paulo Cesar C., Savi, Marcelo A., Netto, Theodoro Antoun, Pacheco, Pedro Manuel C.L., 2009. A phenomenological description of the thermomechanical coupling and the rate-dependent behavior of shape memory alloys. J. Intell. Mater. Syst. Struct. 20 (14), 1675–1687.

Moumni, Z, Herpen, A Van, Riberty, P, 2005. Fatigue analysis of shape memory alloys: energy approach. Smart Mater. Struct. 14 (5), S287–S292.

Moumni, Ziad, Zhang, Yahui, Wang, Jun, Gu, Xiaojun, 2018. A global approach for the fatigue of shape memory alloys. Shap. Mem. Superelasticity 4 (4), 385–401.

Oliveira, S.A., Savi, M.A., Santos, I.F., 2014. Uncertainty Analysis of a One-dimensional Constitutive Model for Shape Memory Alloy Thermomechanical Description. International Journal of Applied Mechanics 6 (6), 1450067.

Oliveira, Sergio A., Savi, Marcelo A., Zouain, Nestor, 2016. A three-dimensional description of shape memory alloy thermomechanical behavior including plasticity. J Braz. Soc. Mech. Sci. Eng. 38 (5), 1451–1472.

Oliveira, Sergio de A., Dornelas, Vanderson M., Savi, Marcelo A., Pacheco, Pedro Manuel C.L., Paiva, Alberto, 2018. A phenomenological description of shape memory alloy transformation induced plasticity. Meccanica 53 (10), 2503–2523.

Paiva, Alberto, Savi, Marcelo Amorim, Braga, Arthur Martins Barbosa, Pacheco, Pedro Manuel Calas Lopes, 2005. A constitutive model for shape memory alloys considering tensile–compressive asymmetry and plasticity. Int. J. Solids Struct. 42 (11-12), 3439–3457.

Paiva, Alberto, Savi, Marcelo Amorim, 2006. An overview of constitutive models for shape memory alloys. Math. Prob. Eng. 2006, 1–30.

Pelton, A.R., 2011. Nitinol fatigue: a review of microstructures and mechanisms. J. Mater. Eng. Perform. 20 (4-5), 613–617.

Petrini, L., Migliavacca, F., 2011. Biomedical applications of shape memory alloys. J. Metal.. 1–15, 2011.

Phillips, Francis R., Wheeler, Robert W., Geltmacher, Andrew B., Lagoudas, Dimitris C., 2019. Evolution of internal damage during actuation fatigue in shape memory alloys. Int. J. Fatigue 124, 315–327.

Predki, W., Klönne, M., Knopik, A., 2006. Cyclic torsional loading of pseudoelastic NiTi shape memory alloys: damping and fatigue failure. Mater. Sci. Eng., A 417 (1–2), 182–189.

Qin, X., Zhang, X., Yan, X., et al., 2019. Structural and functional fatigue behavior of Ni49.8Ti50.2 (at. %) wires under various maximum heating temperatures: experimental and modeling study. Mater. Des. 178, 107842.

Qiu, Bo, Kan, Qianhua, Kang, Guozheng, Yu, Chao, Xie, Xi, 2019. Rate-dependent transformation ratcheting-fatigue interaction of super-elastic NiTi alloy under uniaxial and torsional loadings: Experimental observation. Int. J. Fatigue 127, 470–478.

de Oliveira Ramos, Allysson Daniel, de Araújo, Carlos José, de Oliveira, Henrique Martinni Ramos, Macêdo, Gabriel Almeida, de Lima, Antonio Gilson Barbosa, 2018. An experimental investigation of the superelastic fatigue of NiTi SMA wires. J Braz. Soc. Mech. Sci. Eng. 40 (4). https://doi.org/10.1007/s40430-018-1101-0.

Runciman, Amanda, Xu, David, Pelton, Alan R., Ritchie, Robert O., 2011. An equivalent strain/Coffin–Manson approach to multiaxial fatigue and life prediction in superelastic Nitinol medical devices. Biomaterials 32 (22), 4987–4993.

Song, Di, Kang, Guozheng, Kan, Qianhua, Yu, Chao, Zhang, Chuanzeng, 2015a. Non-proportional multiaxial whole-life transformation ratchetting and fatigue failure of super-elastic NiTi shape memory alloy micro-tubes. Int. J. Fatigue 80, 372–380.

Song, Di, Kang, Guozheng, Kan, Qianhua, Yu, Chao, Zhang, Chuanzeng, 2015b. Damage-based life prediction model for uniaxial low-cycle stress fatigue of super-elastic NiTi shape memory alloy microtubes. Smart Mater. Struct. 24 (8), 085007. https://doi.org/10.1088/0964-1726/24/8/085007.

Song, Di, Kang, Guozheng, Yu, Chao, Kan, Qianhua, Zhang, Chuanzeng, 2017. Non-proportional multiaxial fatigue of super-elastic NiTi shape memory alloy micro-tubes: damage evolution law and life-prediction model. Int. J. Mech. Sci. 131-132, 325–333.

Sgambitterra, Emanuele, Magarò, Pietro, Niccoli, Fabrizio, Renzo, Danilo, Maletta, Carmine, 2019. Novel insight into the strain-life fatigue properties of pseudoelastic NiTi shape memory alloys. Smart Mater. Struct. 28 (10), 10LT03. https://doi.org/10.1088/1361-665X/ab3df1.

Suresh, S., 1998. Fatigue of Materials. Cambridge University Press, Cambridge.

Tobushi, H., Nakahara, T., Shimeno, Y., et al., 2000. Low-cycle fatigue of TiNi shape memory alloy and formulation of fatigue life. ASME. J. Eng. Mater. Technol. 122 (2), 186–191.

Tyc, O., Pilch, J., Sittner, P., 2016. Fatigue of superelastic NiTi wires with different plateau strain. Procedia Struct. Integrity 2, 1489–1496.

Viet, Nguyen Van, Zaki, Wael, Moumni, Ziad, 2019. A model for shape memory alloy beams accounting for tensile compressive asymmetry. J. Intell. Mater. Syst. Struct. 30 (18-19), 2697–2715.

Yamauchi, K., Ohkata, I., Tsuchiya, K., Miyazaki, S. (Eds.), 2011. Shape memory and superelastic alloys. Woodhead Publishing Limited.

Zhang, Yahui, Zhu, Jihong, Moumni, Ziad, Van Herpen, Alain, Zhang, Weihong, 2016a. Energy-based fatigue model for shape memory alloys including thermomechanical coupling. Smart Mater. Struct. 25 (3), 035042. https://doi.org/10.1088/0964-1726/25/3/035042.

Zhang, Xiaoyong, Huang, Dawei, Yan, Xiaojun, Zhou, Xu, 2016b. Modeling functional fatigue of SMA using a more accurate subdivision of martensite volume fractions. Mech. Mater. 96, 12–29.

Zhang, Yahui, You, Yajun, Moumni, Ziad, Anlas, Gunay, Zhu, Jihong, Zhang, Weihong, 2017. Experimental and theoretical investigation of the frequency effect on low cycle fatigue of shape memory alloys. Int. J. Plast. 90, 1–30.

Zhang, Yahui, You, Yajun, Moumni, Ziad, Anlas, Gunay, Zhu, Jihong, Zhang, Weihong, 2019. Stored-energy-based fatigue criterion for shape memory alloys. Smart Mater. Struct. 28 (6), 065027. https://doi.org/10.1088/1361-665X/ab18b0.

Zheng, Lin, He, Yongjun, Moumni, Ziad, 2017. Investigation on fatigue behaviors of NiTi polycrystalline strips under stress-controlled tension via in-situ macro-band observation. Int. J. Plast. 90, 116–145.